



PACE Technical Report Series, Volume 4

Ivona Cetinić, Charles R. McClain, and P. Jeremy Werdell, Editors

Cloud Retrievals in the PACE Mission: PACE Science Team Consensus Document

*Steve Platnick, Odele Coddington, Steven A. Ackerman, Richard Frey, Andrew Heidinger, Andi Walter,
Kerry G. Meyer, Zhibo Zhang, and Bastiaan van Diedenhoven*

National Aeronautics and
Space Administration

**Goddard Space Flight Center
Greenbelt, Maryland 20771**

NASA STI Program ... in Profile

Since its founding, NASA has been dedicated to the advancement of aeronautics and space science. The NASA scientific and technical information (STI) program plays a key part in helping NASA maintain this important role.

The NASA STI program operates under the auspices of the Agency Chief Information Officer. It collects, organizes, provides for archiving, and disseminates NASA's STI. The NASA STI program provides access to the NASA Aeronautics and Space Database and its public interface, the NASA Technical Report Server, thus providing one of the largest collections of aeronautical and space science STI in the world. Results are published in both non-NASA channels and by NASA in the NASA STI Report Series, which includes the following report types:

- **TECHNICAL PUBLICATION.** Reports of completed research or a major significant phase of research that present the results of NASA Programs and include extensive data or theoretical analysis. Includes compilations of significant scientific and technical data and information deemed to be of continuing reference value. NASA counterpart of peer-reviewed formal professional papers but has less stringent limitations on manuscript length and extent of graphic presentations.
- **TECHNICAL MEMORANDUM.** Scientific and technical findings that are preliminary or of specialized interest, e.g., quick release reports, working papers, and bibliographies that contain minimal annotation. Does not contain extensive analysis.
- **CONTRACTOR REPORT.** Scientific and technical findings by NASA-sponsored contractors and grantees.
- **CONFERENCE PUBLICATION.** Collected papers from scientific and technical conferences, symposia, seminars, or other meetings sponsored or co-sponsored by NASA.
- **SPECIAL PUBLICATION.** Scientific, technical, or historical information from NASA programs, projects, and missions, often concerned with subjects having substantial public interest.
- **TECHNICAL TRANSLATION.** English-language translations of foreign scientific and technical material pertinent to NASA's mission.

Specialized services also include organizing and publishing research results, distributing specialized research announcements and feeds, providing help desk and personal search support, and enabling data exchange services. For more information about the NASA STI program, see the following:

- Access the NASA STI program home page at <http://www.sti.nasa.gov>
 - E-mail your question via the Internet to help@sti.nasa.gov
 - Phone the NASA STI Information Desk at 757-864-9658
 - Write to:
NASA STI Information Desk
Mail Stop 148
NASA's Langley Research Center
Hampton, VA 23681-2199
-



PACE Technical Report Series, Volume 4

Editors:

Ivona Cetinić

GESTAR/Universities Space Research Association, Columbia, Maryland

Charles R. McClain

Science Applications International Corporation, McLean, Virginia

P. Jeremy Werdell

NASA Goddard Space Flight Center, Greenbelt, Maryland

Cloud Retrievals in the PACE Mission: PACE Science Team Consensus Document

Steve Platnick

NASA Goddard Space Flight Center, Greenbelt, Maryland

Odele Coddington

University of Colorado, Boulder, Colorado

Steven A. Ackerman

University of Wisconsin, Madison, Wisconsin

Richard Frey

University of Wisconsin, Madison, Wisconsin

Andrew Heidinger

University of Wisconsin, Madison, Wisconsin/NOAA, Madison, Wisconsin

Andi Walter

University of Wisconsin, Madison, Wisconsin

Kerry G. Meyer

NASA Goddard Space Flight Center, Greenbelt, Maryland

Zhibo Zhang

University of Maryland, Baltimore County, Baltimore, Maryland

Bastiaan van Diedenhoven

Columbia University /NASA Goddard Institute for Space Studies, New York, NY

National Aeronautics and
Space Administration

Goddard Space Flight Center
Greenbelt, Maryland 20771

Notice for Copyrighted Information

This manuscript has been authored by employees of *GESTAR/Universities Space Research Association, and Science Applications International Corporation, University of Wisconsin, Columbia University* with the National Oceanic and Atmospheric Administration and the National Aeronautics and Space Administration. The United States Government has a nonexclusive, irrevocable, worldwide license to prepare derivative works, publish or reproduce this manuscript for publication acknowledges that the United States Government retains such a license in any published form of this manuscript. All other rights are retained by the copyright owner.

Trade names and trademarks are used in this report for identification only. Their usage does not constitute an official endorsement, either expressed or implied, by the National Aeronautics and Space Administration.

Level of Review: This material has been technically reviewed by technical management.

Available from

NASA STI Program
Mail Stop 148
NASA's Langley Research Center
Hampton, VA 23681-2199

National Technical Information Service
5285 Port Royal Road
Springfield, VA 22161
703-605-6000

Available in electronic form at <http://>

PREFACE

Introduction

The Plankton, Aerosol, Cloud, ocean Ecosystem (PACE; <https://pace.gsfc.nasa.gov>) mission's first completed PACE Science Team was formed in 2015 and spanned three years. This first team was tasked with collaboratively documenting the current state-of-the-art in passive satellite retrieval of marine inherent optical properties (IOPs) and ocean color atmospheric correction (AC), with the goal of laying a foundation for future PACE-related research and algorithm development. Proposers applied for membership on either the IOP or AC team. Science team members ultimately pursued their own proposed research, but they also collaborated with their team in the development of consensus documents that described the state-of-the-art in their discipline as it related to the expected capabilities of the PACE observatory.

Ultimately, the AC team further organized themselves into three sub-groups focused on ocean color atmospheric correction, aerosol retrievals, and cloud retrievals with each sub-group pursuing an independent consensus document. This volume presents the PACE Science Team consensus document on the cloud retrieval capabilities of the PACE mission. Retrievals from both the PACE spectrometer (Ocean Color Instrument) and a multi-angle polarimeter are explored.

My thanks go out to the first PACE Science Team for their collaborative good nature and enthusiasm in developing these documents. The energy expended in their development will ultimately benefit a broad community as an exceptional resource and further highlight the multi-disciplinary collaboration being pursued in the formulation of the PACE mission.

P. J. Werdell
PACE Project Scientist
June 2018

Table of Contents

1. Introduction	5
2. Cloud Properties from PACE OCI.....	7
2.1. Cloud Detection and Masking from OCI.....	7
2.2. Cloud Top Height from OCI.....	9
2.3. Cloud Thermodynamic Phase and Cloud Optical Properties from OCI.....	19
2.4. Cloud Spatial Resolution Sensitivities with OCI	24
3. Cloud Properties from a Notional PACE Polarimeter	30
3.1. Liquid Water Cloud Polarimetric Retrievals.....	30
3.2. Ice Cloud Polarimetric Retrievals	35
3.3. Cloud Thermodynamic Phase from Polarimetry.....	37
4. References	38

Chapter 1

1. Introduction

Importance: Earth is a complex dynamical system exhibiting continuous change in its atmosphere, ocean, and surface elements. Nearly all (99.97%) of the energy driving these systems is linked to the Sun. Measurements of reflected sunlight contain a unique signature of wavelength-specific scattering and absorption interactions occurring between incoming solar energy and atmospheric (molecules, aerosols, clouds) and surface features.

Clouds can affect significantly both shortwave and longwave radiation, depending on altitude/vertical structure, thermodynamic phase, and optical properties. Low, warm, and optically thick clouds predominantly have a cooling effect, while high, cold, optically thin clouds can cause warming by absorbing warmer radiation emitted from the surface and lower atmosphere.

When the net difference between outgoing and incoming solar radiation is matched by the net infrared radiation emitted to space, the Earth's climate is in radiative balance. While radiative forcing components (GHGs, aerosols—direct and indirect) contribute to a net radiative imbalance, climate sensitivity is ultimately determined by the contribution of various system feedbacks. The role of cloud feedback in a warming climate is currently the largest inter-model uncertainty in climate sensitivity and therefore in climate prediction [Bony and Dufresne 2005]. A comprehensive understanding of current cloud properties and dynamic/microphysical processes requires a global perspective from satellites.

Challenges with current imagers: Active sensors have provided unique observations of cloud structure in recent years (CALIPSO, CloudSat). However, modern passive imagers provide unique information on optical/radiative properties and have/will comprise a multi-decadal data record (e.g., 17 and 15 years for EOS Terra and Aqua MODIS, respectively, to date and well into the 2030s with SNPP and JPSS-1, -2, etc.). However, obtaining cloud climate data records from the current generation of global imagers (MODIS, VIIRS) is challenging due to the need for exacting reflectance stability over multiple decades [Franz et al., 2008; Levy et al., 2010; Sun et al., 2012a,b; Lyapustin et al., 2014].

Therefore, an overriding interest in OCI for cloud team members is in achieving unprecedented instrument stability for climate observations. To date, the stability of MODIS reflectometry for the quantification of climate trends is in doubt for several key data records (see above references) while the eventual long-term stability or radiometry of VIIRS solar reflectance channels with respect to MODIS is not yet known [Wang and Cao, 2016; Xiong et al., 2016; Sayer et al., 2016]. Imager stability requirements for ocean color applications have been demonstrated to the sub-percent level for SeaWiFS using lunar observations [Eplee et al., 2011], and similar capabilities are expected for OCI. Therefore, it is of strategic interest to NASA and the community to understand the extent to which a PACE ocean color imager can be used to produce relevant and stable cloud products.

The cloud case for PACE: The PACE Ocean Color Instrument (OCI), will contribute to the global cloud data record by providing information in key spectral VNIR and SWIR spectral channels that have heritage with MODIS and VIIRS. PACE OCI cloud property products will include cloud amount, cloud pressure/altitude, thermodynamic phase, optical thickness, and effective particle size. PACE is also expected to fly a multispectral and Multi Angle Polarimeter (MAP). Depending on the combination of spectral and angular sampling available with MAP, unique capabilities for cloud top phase discrimination and microphysical information (effective size and variance) may be possible.

Challenges with PACE: The PACE mission will not have infrared channels that historically have been used along with solar reflectance channels to retrieve the aforementioned cloud properties. Converting the individual cloud property datasets into a climate data record carries additional challenges that have already been recognized for the existing individual satellite data records that are due to differences in instrument design (such as measurement channel centers and spectral resolutions), instrument on-orbit stability, and instrument operations.

Table 1.1. Principle channels for cloud product studies used by the PACE cloud team (taken from PACE Science Definition Team [2018]).

Central Wavelength (nm)
665
865
763
940
1240
1378
1640
2135
2250

2. Cloud Properties from PACE OCI

The NASA global imagers, MODIS and VIIRS, are the current generation of imagers for global studies. The notional PACE OCI instrument is expected to have improved on-orbit stability and measurement precision than the MODIS or VIIRS instrument. Therefore, the OCI instrument is valuable for improving the utility of MODIS and VIIRS cloud products for climate studies.

The lack of infrared channels on PACE OCI is the chief limiting factor for achieving cloud record continuity with daytime observations by MODIS/VIIRS and other heritage sensors. MODIS and VIIRS use infrared channels for cloud detection and masking, deriving cloud top properties (cloud top pressure, temperature, and effective cloud amount), cloud thermodynamic phase, cloud optical properties (droplet effective radius) and derived cloud water path, and other metrics designed to identify failed retrievals and to quantify retrieval uncertainties.

The following subsections discuss the advantages and limitations of deriving cloud properties from PACE OCI with respect to the MODIS and VIIRS imagers. Useful comparisons in evaluating PACE OCI cloud retrieval uncertainties towards understanding and achieving cloud product continuity with MODIS and VIIRS requires utilizing the existing NASA MODIS/VIIRS algorithms, to the extent possible. In some cases, such as deriving cloud-top information from the O2-A band and water vapor bands and deriving cloud thermodynamic phase from shortwave-infrared (SWIR) channels only, we also discuss new algorithms that have been developed to utilize the additional information the PACE OCI provides.

2.1. Cloud Detection and Masking from OCI

Clouds are generally characterized by higher reflectivities and lower temperatures than the underlying surface of the earth. Simple visible, near-infrared (NIR), and longwave infrared (LWIR) threshold tests for clouds often show considerable skill in discriminating between clear and cloudy skies. However, there are some surfaces where this characterization of clouds is inappropriate, most notably over snow and ice. Additionally, some cloud types such as thin cirrus and small-scale cumulus are difficult to detect because of insufficient contrast with surface radiances. Cloud edges also increase difficulty since the instrument field of view is not completely cloudy or completely clear.

Development of the PACE OCI cloud mask algorithm benefits from previous work to characterize global cloud cover using satellite observations. The International Satellite Cloud Climatology Project (ISCCP) developed cloud detection schemes using visible and infrared window radiances [Rossow and Garder, 1993]. The Clouds from AVHRR (Advanced Very High Resolution Radiometer) Extended (CLAVER-x) system [Heidinger *et al.*, 2012] is NOAA's operational cloud processing system for the AVHRR on the NOAA-POES and EUMETSAT-METOP series of satellites and uses six Bayesian classifiers computed separately for seven surface types. The overall result is given as the probability of cloud contamination (0.0–1.0) rather than as a yes/no decision. The MODIS Cloud Mask, known as MOD35 [Ackerman, *et al.*, 1998], uses 19 spectral bands in a fuzzy logic thresholding algorithm. This algorithm results in a clear sky confidence (0.0–1.0) for each pixel and reports one of four possible categories; confident clear (>0.99), probably clear (>0.95), probably cloud (>0.66), and confident cloud (≤ 0.66). CO₂ slicing, used for multi-decadal HIRS processing [Menzel *et al.*, 2016] and decade-plus MODIS data [Menzel *et al.*, 2008], characterizes global high cloud cover, including thin cirrus, using infrared radiances in the

carbon dioxide absorption region of the LWIR spectrum. More recently, efforts to maintain continuity from MODIS to VIIRS instruments have resulted in the MODIS-VIIRS Cloud Mask (MVCM, in development) that features MODIS-like methodology but uses only those channels common to both sensors.

The PACE OCI cloud mask will follow the MOD35 and MVCM methodologies and report a confidence of clear sky for each pixel during daylight conditions. A complicating factor for the OCI mask is that the instrument lacks infrared channels with wavelengths greater than 2250 nm. Longwave IR measurements are useful for: 1) detecting cold but highly reflective clouds over bright surfaces like snow, sun-glint, or deserts; 2) detecting relatively “dim” clouds over dark surfaces like small-scale cumulus clouds or when pixels contain only scattered clouds; 3) creating brightness temperature differences between wavelengths characterized by differing atmospheric absorption and/or cloud particle emission characteristics (e.g., 11–12 μm for thin cirrus detection).

On the positive side, the OCI will have a single-science-pixel rotating scanner to avoid multi-detector striping and will be tilted at a 20-degree angle in the forward or backward direction to minimize the ocean surface area impacted by sun glint. It is also the case that for dark surfaces like oceans and heavily vegetated lands, use of visible (0.65 μm , land) and NIR (0.86 μm , water) reflectances alone can detect a very high fraction of the total clouds (see **Fig. 2.1**). Additionally, development work has shown that use of the 1.64- μm channel over oceans is very sensitive to thin water clouds and partial cloudiness in the boundary layer due to very dark surface reflectances at this wavelength. The 1.38- μm channel is very useful for detection of transmissive cirrus clouds, especially where atmospheric moisture is plentiful through a deep layer of the troposphere. Use of 3 \times 3-pixel variability measures over water surfaces is also a promising route to better discriminate clear vs. cloudy skies where LWIR data is not available. Currently, the MOD35 and MVCM nighttime ocean algorithms use an 11- μm variability test that could be modified for daytime applications in visible and/or NIR spectral bands.

Effective cloud screening will be challenging over many land surface types. Making cloud test thresholds functions of the Normalized Difference Vegetation Index (NDVI) can help in those regions where a majority of the surface is covered by vegetation, though much of the land surface area of the globe is covered by arid and semi-arid ecosystems where knowledge of the skin temperature and use of LWIR brightness temperature differences is crucial for high quality cloud masking.

Snow and ice cover present another set of problems. The Normalized Difference Snow Index (NDSI) [Hall, *et al.*, 1995] is a good discriminator between water clouds and snow/ice but can display ambiguous values when ice phase clouds are present. In these cases, especially in non-polar regions, use of LWIR data is very useful in discriminating between high altitude cirrus or multi-layered clouds and snow/ice surfaces.

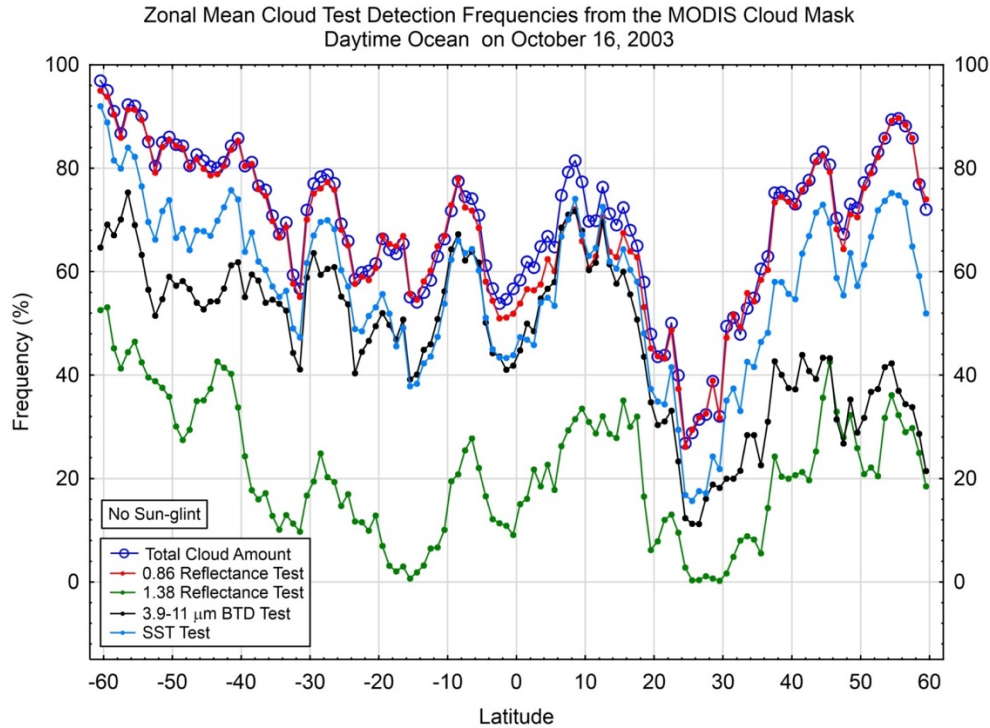


Figure 2.1. Zonal mean daytime ocean MOD35 total cloud detection frequency (larger open circles) and individual cloud test detection frequencies (smaller filled circles) on October 16, 2003. Some zones show slightly more cloud detected by the 0.86- μm test than the algorithm total. These are accounted for by clear sky restoral tests where original cloudy determinations are reversed to clear if certain spatial variability or other non-ambiguous spectral clear sky criteria are met.

2.2. Cloud Top Height from OCI

Estimates of cloud height using space-borne sensors have a long lineage, and notably include well characterized techniques using observations in thermal infrared (IR) spectral channels. Among these are IR window techniques that provide direct estimates of cloud temperature and the CO_2 slicing technique from which cloud pressure can be estimated from the differential absorption of IR channels inside and outside the $15\mu\text{m}$ CO_2 absorption region; cloud altitude can be derived from both techniques if the atmospheric profile of temperature and pressure is known. Because OCI will not include thermal infrared channels, however, other means of estimating cloud altitude will be pursued, namely those exploiting solar spectral channels inside and outside the H_2O [e.g., Meyer *et al.*, 2010; Wang *et al.*, 2012] and O_2 A-band [e.g. Fischer and Grassl, 1991; Wang *et al.*, 2008] absorption regions. The sensitivity to cloud altitude of these spectral channels lies in the attenuation of the top of atmosphere (TOA) cloud reflectance due to atmospheric gas absorption. Computing the ratio of the TOA reflectance of a gas absorbing channel to that of a window channel in close spectral proximity, coupled with knowledge of both the profile of the atmospheric gas absorber and the spectral dependence of cloud-top reflection, allows for estimates of cloud altitude.

Cloud altitude derived from solar absorption techniques can be notably different from that derived from IR techniques, however, a difference that results from the vertical sensitivity within the cloud of the respective spectral regimes. IR observations are sensitive to the effective level of emission within the cloud when the cloud is opaque, which is near an optical depth of unity from the physical cloud top. Solar reflectance measurements, on the other hand, are sensitive to the effective level of scattering which can be

much deeper into the cloud than the effective level of emission, depending on the strength of the absorber, and thus retrievals of cloud altitude can be much lower. Nevertheless, such solar cloud altitude retrievals, particularly the O₂ A-band technique, are well understood and have been utilized on other space-borne platforms such as DSCOVR-EPIC, POLDER and MERIS.

The OCI level-1 requirements include several solar spectral channels within gas absorption regions that can be used to help estimate cloud altitude. **Table 2.2** lists the channels relevant to the notional cloud top properties retrieval algorithm described later and the main absorbers.

Table 2.2. OCI spectral channels relevant to the notional cloud top properties algorithm along with the spectral widths assumed for this study.

OCI CWL (μm)	Full Width Half Maximum (nm)	Primary Absorber
0.76	5	O ₂
0.86	40	Window
0.94	25	H ₂ O
1.24	20	Window
1.38	10	H ₂ O

Figure 2.2 (below) provides a summary of the information content of the channels in the above table, namely the reflectance ratio weighting functions. The weighting functions are the derivative, or slope, of the reflectance ratios with pressure, and are a function of the strength of absorption and the vertical profile of the absorber. The greater the value of the slope, the stronger the sensitivity to cloud height. The O₂ A-band ratio (0.76/0.86 μm) shows moderate values throughout the atmosphere, and exhibits a linear behavior because O₂ is a uniformly mixed gas and this channel realization does not saturate (i.e., is sensitive to low levels in the atmosphere). The 1.38/1.24-μm ratio provides very high sensitivity in the upper troposphere and little information at lower levels due to the strong H₂O absorption at 1.38 μm. The 0.94/0.86 μm ratio, located in a less absorbing H₂O band, provides very complementary information at mid-levels in the atmosphere. Of course, the weighting functions for the 1.38 and 0.94 μm ratios will vary with the moisture of the atmosphere, though for almost any atmosphere we would expect 1.38 μm to provide useful information even when the surface signal at 1.38 μm is not completely attenuated. Moreover, while the figure implies the utility of the 0.76-μm channel is negligible compared to the H₂O channels, it is important to realize that the O₂ concentration uncertainties are much lower than those of the more variable H₂O profile, and the relative contribution of the 0.76-μm channel is expected to be larger than is shown here; likewise, in drier atmospheres the 0.76 μm channel will be of greater importance. Given the sensitivities of the ratios in **Fig. 2.2**, it is expected that the notional OCI channels in **Table 2.2** have sufficient information content to capture the cloud-top information.

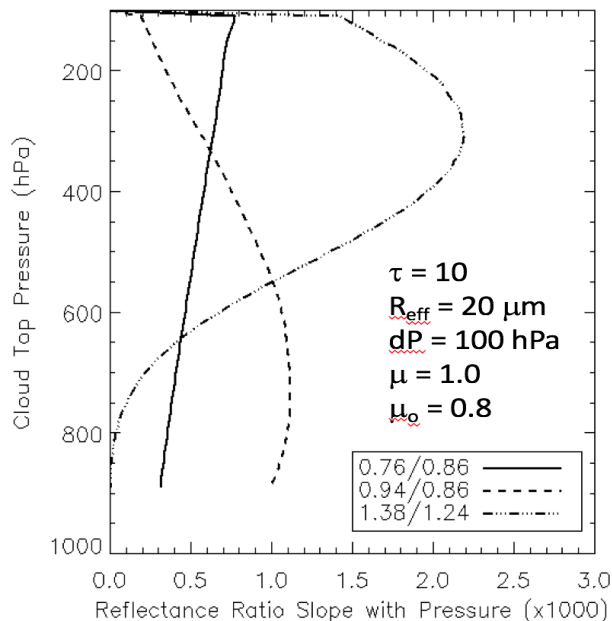


Figure 2.2. Clear-sky weighting functions for the OCI observations used in the notional cloud-top properties retrieval. A standard tropical atmosphere was assumed, with COT and CER set to 10 and 20 μm , respectively.

Radiative Transfer Modelling

To support the development of the PACE cloud top properties algorithm, the CIMSS Correlated- k (CICKER) model, based on the previously developed Successive Order of Interaction (SOI) model [Heidinger, 2006], was modified to support notional OCI channels. This radiative transfer model uses an adding/doubling radiative transfer solver coupled with the correlated- k method to account for atmospheric gaseous absorption. The correlated- k fitting was performed for the channels in **Table 2.2** assuming a Gaussian spectral response function and the full width half maximum (FWHM) values shown. The adding/doubling solver can treat both thermal and solar sources and can handle an arbitrary number of atmospheric layers. Each layer can have water cloud, ice cloud, or aerosol (e.g., dust, smoke, volcanic ash), though only up to two cloud layers can be defined within a given profile. The cloud bulk scattering phase functions are generated by fitting Mie scattering results for liquid water clouds and severely roughened aggregate column crystals [Yang *et al.*, 2013] for ice clouds. Mixed phase clouds can be constructed by placing ice and water clouds at the same levels. The vertical profile of effective radius within the cloud can be homogenous, vary linearly, or vary to give a constant liquid water content throughout the cloud.

A validation study of the correlated- k fits used in CICKER was performed. **Table 2.3** shows the nadir transmission values (one-way) for the three key OCI cloud-top properties absorbing channels. The results show that CICKER adequately characterizes the gaseous absorption in each channel over a wide range of absorber amounts; column water amounts are indicated under each profile name. Because O_2 is a well-mixed gas, the 0.76 μm results do not change with the atmospheric profile and are a function only of the surface pressure. CICKER does show systematic transmission bias and this might be due to lack of treatment of H_2O continuum in this spectral region.

Table 2.3. Nadir one-way transmission values for selected OCI bands computed for standard atmospheres from MODTRAN-4 and CICKER.

Channel	TROPICAL (42mm H ₂ O)		MID LAT SUM (30mm H ₂ O)		SUB-ARCTIC SUM (21.1mm H ₂ O)		SUB-ARCTIC WIN (4.2mm H ₂ O)	
	MOD4	CICKER	MOD4	CICKER	MOD4	CICKER	MOD4	CICKER
0.76	0.57	0.56	0.57	0.56	0.57	0.56	0.57	0.56
0.94	0.35	0.37	0.42	0.44	0.48	0.51	0.75	0.78
1.38	0.001	0.00006	0.0033	0.0006	0.48	0.51	0.135	0.125

Sensitivity Analysis

To illustrate the sensitivity of the OCI channels in **Table 2.3** to cloud top pressure (CTP), two idealized cloud cases were simulated using the CICKER radiative transfer model, namely a single layer ice cloud and a multilayer scenario with an ice cloud overlying a low-level liquid water cloud. For both scenarios, the atmosphere has a column water vapor amount of 25 mm and a scale height of 2 km. The atmospheric lapse rate is 6 K/km. The sun is directly overhead (i.e., solar zenith angle 0°), and the view zenith angle is 30°.

The results of the single layer ice cloud simulations are shown in **Fig. 2.3**. Panels (a) through (e) show the TOA reflectance (in percent) at each of the five channels in **Table 2.2** as a function of CTP and the vertical pressure thickness of the cloud. For this example, cloud optical thickness (COT) and effective radius (CER) are fixed at 4 and 20 μm, respectively. The large reflectance variation exhibited by the three absorbing channels (0.75, 0.94, 1.38 μm) across the horizontal indicates the sensitivity of these channels to CTP, while the reference window channels (0.86, 1.24 μm) exhibit nearly uniform reflectance (note that the color bar reflectance ranges differ for each channel). The absorbing channel reflectance variation in the vertical also indicates some sensitivity to the cloud pressure thickness, though this sensitivity is much less than that of CTP. Panels (f) to (h) show the distributions of the reflectance ratios. While the reflectance ratio patterns indicate similar sensitivities as the absorbing channel reflectances themselves, the use of ratios is preferred since they mitigate the sensitivity to COT and microphysics relative to CTP (see **Fig. 2.5**). Panel (i) condenses the information conveyed in panels (f) to (h) into a single plot. Here, reflectance ratios are plotted as a function of CTP for three cloud pressure thickness values, namely 160 hPa (solid lines), 24 hPa (upper dashed lines), and 400 hPa (lower dashed lines).

Figure 2.4 shows the same analysis, but with the addition of an underlying low-level liquid cloud located between 800 and 900 hPa with COT of 10 and effective radius of 13 μm. Single layer forward model assumptions break down in such multilayer situations, and retrieval errors and uncertainty may increase significantly as a result. Here, the sensitivities of the reflectance ratios, especially the 0.76-μm and 0.94-μm ratios, to the CTP of the upper-level ice cloud are greatly reduced (e.g., Fig 2.4 panel (i)) due to the presence of the low-level liquid cloud. Such impacts are inherently a function of the COT of both the upper and lower-level clouds; for instance, the impact of the lower-level cloud will decrease as the COT of the upper level cloud increases. Identifying multilayer cloud scenes need to be an integral component of retrieval quality assessment, not only for the cloud top retrievals but for the subsequent optical property retrievals as well. Nevertheless, it is evident that even in multilayer scenes cloud altitude information is still available, specifically in the 1.38-μm ratio, and further investigation is needed.

One Layer Situation: Cirrus Cloud Properties

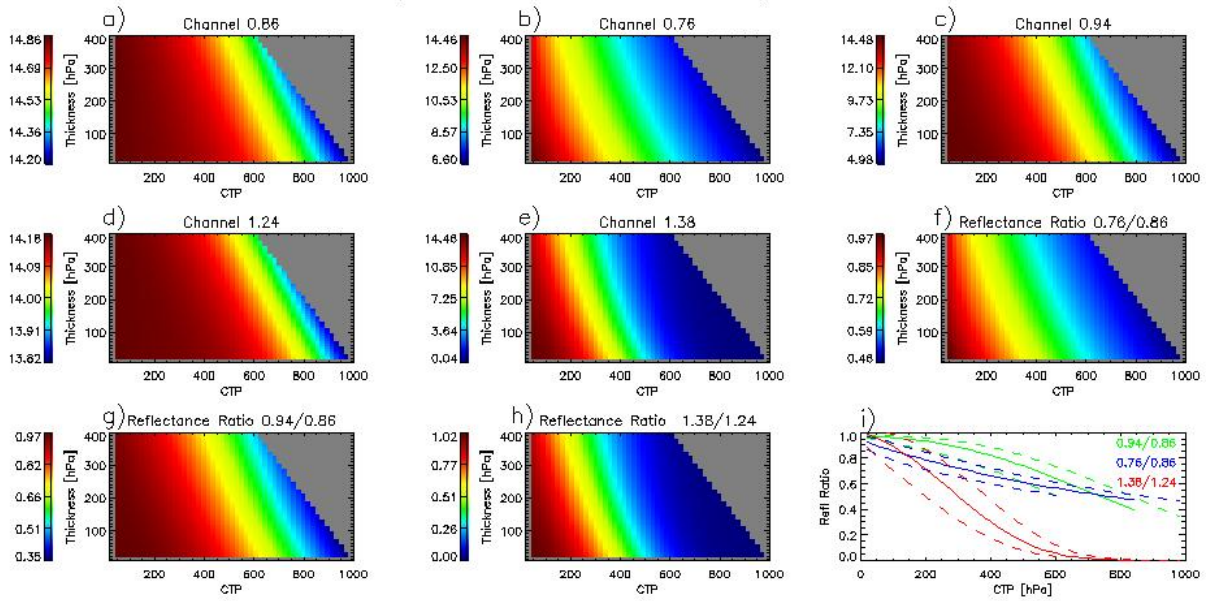


Figure 2.3. A sensitivity study for a single-layer ice cloud. The color bar values represent reflectance (in percent) for the five channels in Table 2.3.2 (panels a-e) and reflectance ratios for three channel combinations (f-h) as a function of cloud-top pressure (CTP) and cloud vertical pressure thickness. Panel (i) shows the reflectance ratios as a function of CTP for three cloud-pressure thicknesses, namely 160 hPa (solid lines), 24 hPa (upper dashed lines), and 400 hPa (lower dashed lines).

Multi Layer Situation: Cirrus Cloud Properties

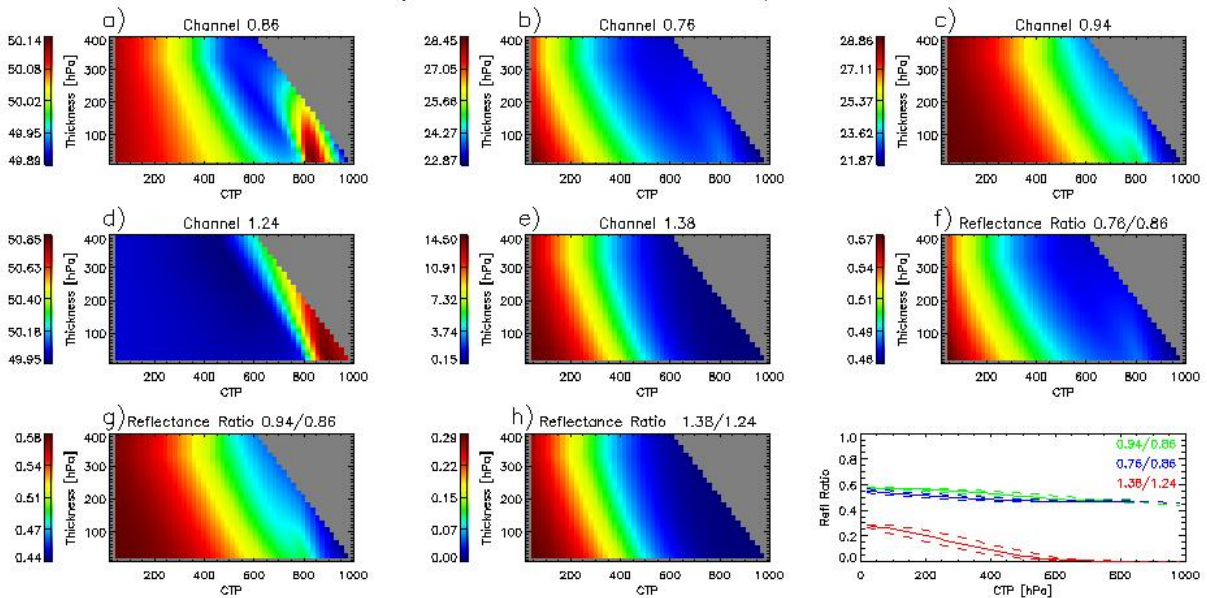


Figure 2.4. The same as Fig. 3.2.3, except with the addition of a low-level liquid cloud between 800 and 900 hPa having optical thickness of 10 and effective radius of 13 μm . The OCI absorbing channels are expected to have reduced sensitivity to the CTP of the upper-level clouds in multilayer cloud scenes, as is shown in panel (i).

Two-Channel Cloud Top Pressure Retrievals

A first-order approach to retrieving cloud altitude from absorbing solar spectral channels is to reduce the solution space to two dimensions to simultaneously infer CTP and COT from the individual reflectance ratios and their respective reference channels. This approach, which resembles the bi-spectral Nakajima-King technique for simultaneous retrievals of COT and effective particle size [Nakajima and King, 1990], requires the assumptions of a fixed cloud vertical thickness and that cloud thermodynamic phase is known. Example solution spaces for the 0.76/0.86 μm (top right), 0.94/0.86 μm (bottom left), and 1.38/1.24 μm (bottom right) reflectance ratios versus their reference channels are shown in **Fig. 2.5**; also shown is the solution space for the 0.76- μm O₂ A-band absorbing channel reflectance versus the 0.86- μm reference channel (top left). Here, the cloud is assumed to be vertically thin (100 hPa thickness) with ice phase and is placed over a dark ocean surface in a tropical atmosphere. The sun is at a zenith angle of 37° and the viewing zenith is at nadir. The solid lines are constant values of COT and the dash-dot lines are constant CTP (labeled P_c in the plot); note that the lower limit of each reflectance ratio is a function of the opacity of the absorbing channel. COT varies from 0.25 to 128 and CTP varies from 150 to 750 hPa. It is evident that the solution spaces are more orthogonal for the reflectance ratios than it is for the absorbing channel reflectance alone, indicating less covariance between CTP and COT. However, while the optical thickness line spacing is similar for each solution space, the spacing of the constant pressure lines does show significant variation; tighter line spacing indicates a reduced sensitivity to CTP. For the 0.76/0.86- μm ratio, the pressure line spacing is relatively constant throughout the troposphere. On the other hand, the 1.38/1- μm ratio results indicate a high sensitivity to CTP in the upper troposphere but much reduced sensitivity in the lower troposphere, while the sensitivity of the 0.94/0.86- μm ratio lies in the mid-levels of the troposphere. These results are consistent with the weighting functions shown in **Fig. 2.2**, and demonstrate the complementary nature of the information content provided by the three reflectance ratios.

Simulated retrieval errors for the reflectance ratio solution spaces of **Fig. 2.5** are shown in **Fig. 2.6**. The left column of panels show the errors for a low liquid phase cloud ($P_c = 750$ hPa) and the right column of panels show the errors for a high ice phase cloud ($P_c = 250$ hPa); each row shows the errors from a single OCI reflectance ratio. The retrieval errors are in units of hPa for CTP (labeled here as P_c) and in percent (%) error for COT. The only perturbation to the simulations was the addition of instrument noise and calibration errors. The instrument terms were added as shown:

$$R_{cont,obs} = (1 + \epsilon/100)R_{cont,true} + \delta$$

$$R_{abs,obs} = (1 + r_c \epsilon/100)R_{abs,true} + r_n \delta$$

Here, R_{cont} refers to window or continuum reflectance (0.86 or 1.24 μm) and R_{abs} refers to the absorbing channel reflectance (0.76, 0.94 or 1.38 μm). ϵ is the calibration error taken to be 5%, and δ is the instrument noise which is assigned a value of 0.1 in reflectance units. r_c is the correlation between the calibration errors in R_{cont} and R_{abs} . For this study, r_c was set to 0.5 meaning the calibration error of the reflectance ratio is half that of the individual reflectances. The r_n value was set to -1.0 meaning the noise is of the opposite sign on each channel, the worst case for noise cancellation. The errors and assumptions seem reasonable, but are likely too simplistic for proper OCI simulations as they are the only errors driving the values in **Fig. 2.6**. Other error sources such as those from atmospheric profile, aerosol, and surface reflectance errors are ignored.

In **Fig. 2.6**, the calibration error dominates the results for COT > 4, and the noise assumptions drive the results for small COT (e.g., cirrus). The COT results show increased errors for thick clouds due to the non-linear relationship between reflectance and optical thickness; note that the error reduction at the largest

COT is an artifact of the sensitivity calculation. The CTP results are consistent with the solution space characteristics shown in **Fig. 2.5**. The CTP errors for high clouds are smallest for the 1.38/1.24- μm ratio; the 0.76/0.86- μm and 0.94/0.86- μm ratios provide similar performance, with errors much larger than those for 1.38/1.24 μm . For the low cloud, the 0.94/0.86- μm results are generally superior to those of the other ratios. The 0.76/0.86- μm ratio provides consistent performance for both the high and low clouds, and performs well for COT > 4 in both cases.

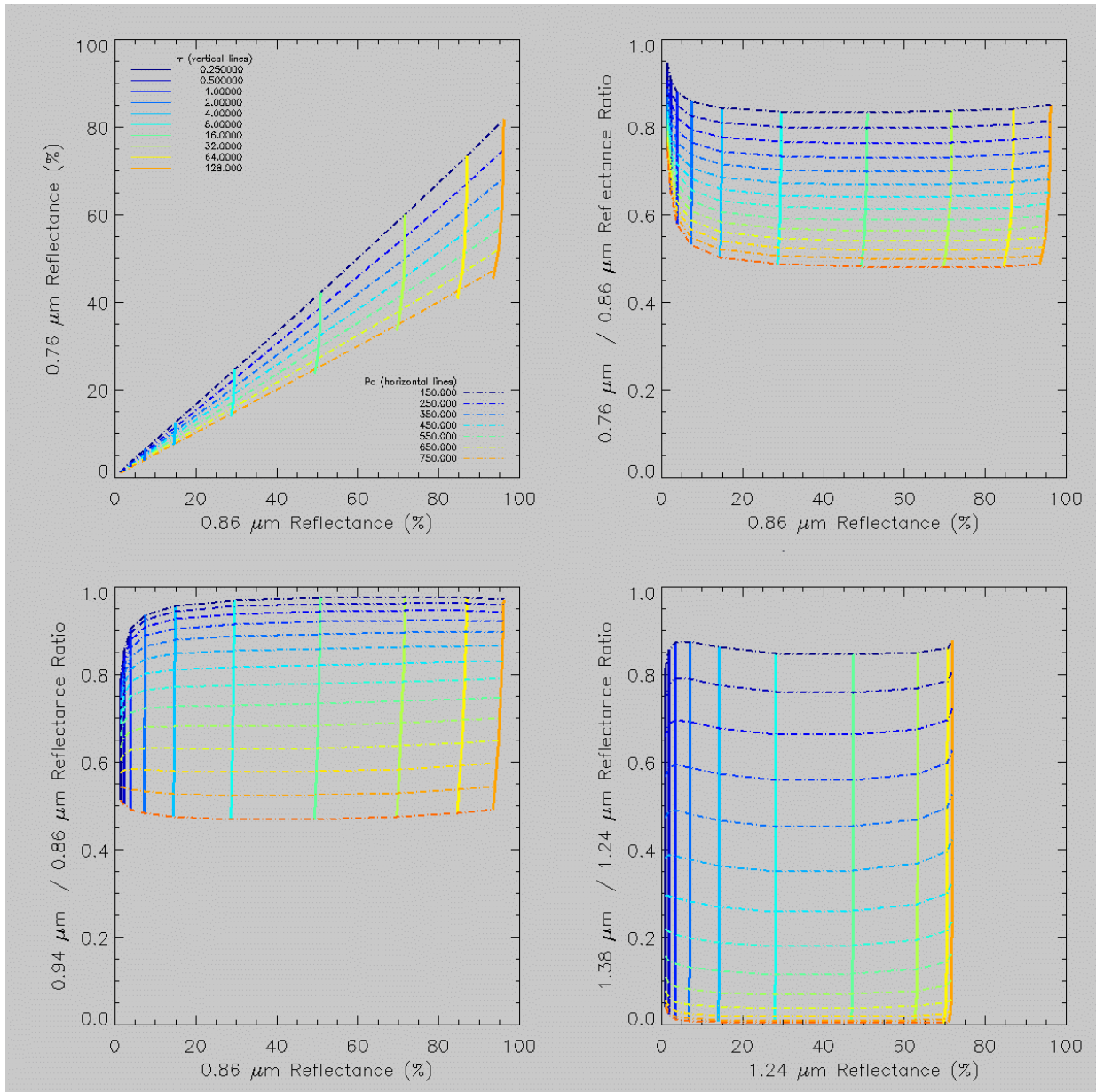


Figure 2.5. The variation of cloud optical depth and cloud-top pressure with the OCI absorbing channel reflectance ratios and their associated reference channel reflectance. Clouds are treated as homogenous layers with a thickness of 100 hPa, embedded in a tropical atmosphere and lying over a dark ocean surface.

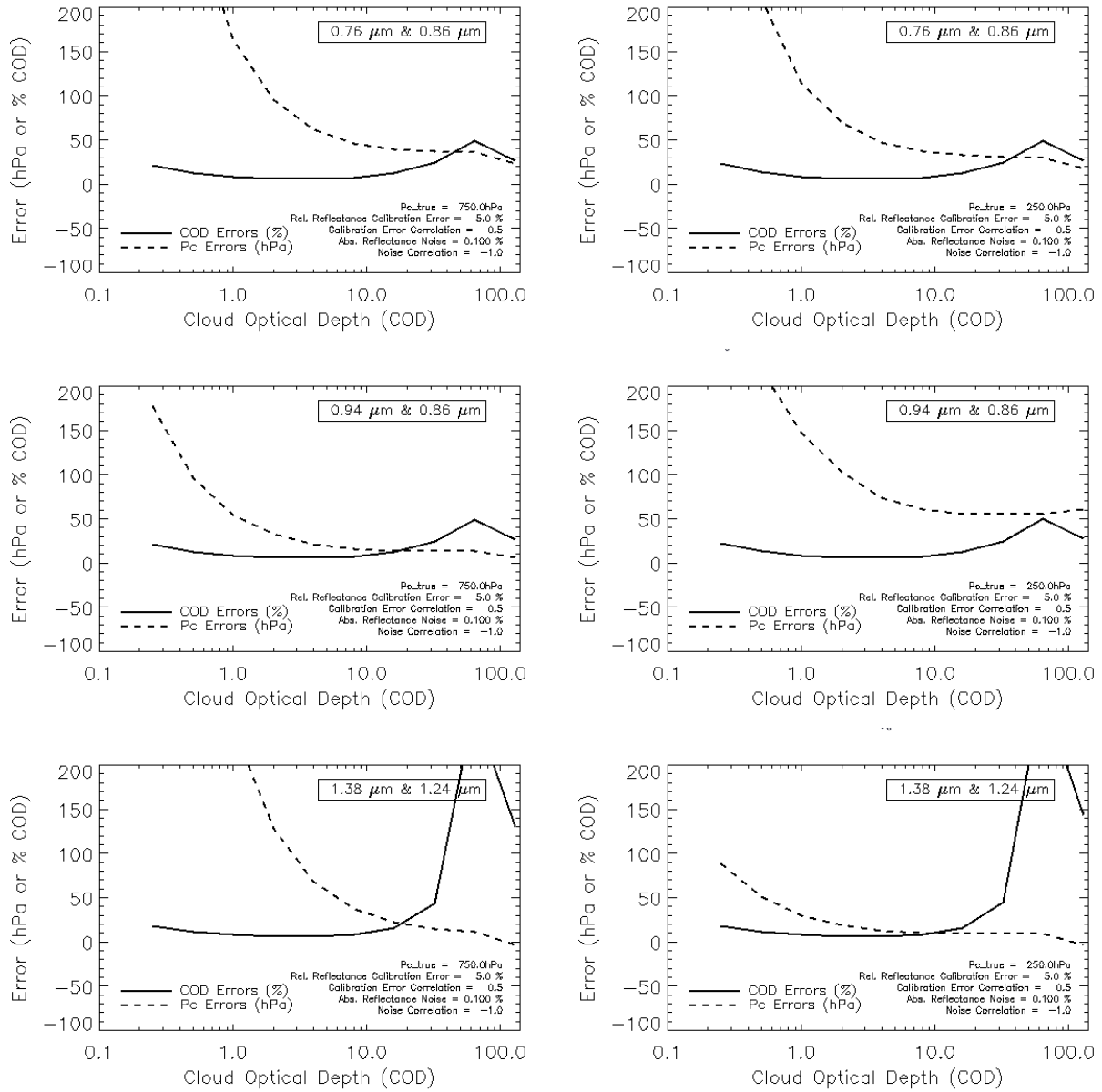


Figure 2.6. Simulated retrieval errors for the data in Fig. 2.5 with an assumed calibration error of 5% and a noise of 0.1% (absolute reflectance). The panels on the left show the results as a function of optical thickness for a cloud with at 750 hPa. The panels on the right show the results as a function of optical thickness for a cloud with at 250 hPa. Errors due to atmospheric profile are ignored.

Multi-Channel Optimal Estimation Retrievals

As the previous section showed, there is significant and complementary information about CTP in the OCI absorbing channels. To efficiently utilize the information content from these channels simultaneously, we have developed an optimal estimation retrieval for COT and CTP, as well as the cloud vertical pressure thickness (Δp). We note that while the primary objective is to provide estimates of CTP, the simulations shown in **Figs. 2.3** and **2.4** indicate additional sensitivity to Δp , so it is included in the state vector here for exploratory purposes. The main advantage of the optimal estimation approach is that it provides a

convenient framework within which to add or remove spectral information from the solution. The solution is found by minimizing the difference between the observations and their estimated values derived from a forward model. The observations used in the notional OCI cloud-top retrieval consist of channel-dependent reflectances or reflectance ratios as follows: [0.86, 0.76/0.86, 0.94/0.86, 1.38/1.24].

The 0.86 μm channel is included to provide sensitivity to COT, and reflectance ratios are used to reduce the sensitivity of the retrieval to calibration errors. The errors of the forward model are the same as those used in the single channel retrievals shown in **Fig. 2.6**, i.e., instrument calibration and noise. The *a priori* values for CTP are 200 hPa for ice clouds and 850 hPa for liquid water clouds. The Δp *a priori* values are 100 hPa for all cloud phases. The *a priori* uncertainties for COT are assumed to be 20%, and for both CTP and Δp are assumed to be 500 hPa; these large CTP and Δp uncertainties imply virtually no skill in the *a priori* estimate. The retrieval assumes the cloud thermodynamic phase is provided by upstream retrievals. As the retrieval matures, these assumptions will be tested and the complexities of error covariance will be studied.

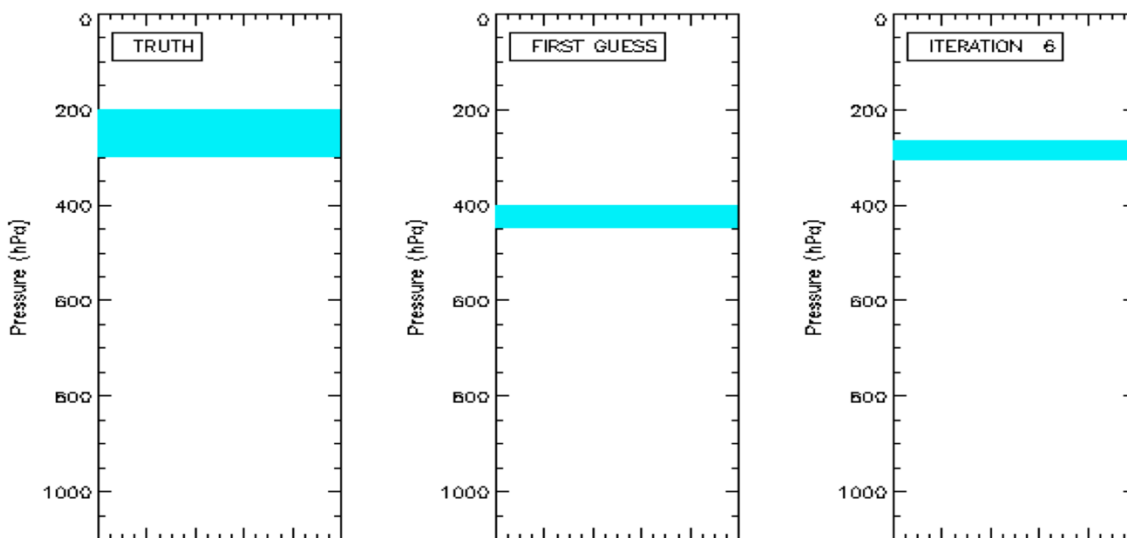


Figure 2.7. Simulated retrieval for a single-layer cloud with CTP = 200 hPa, Δp = 100 hPa, and COT = 10. The *a priori* settings were CTP = 400 hPa, Δp = 50 hPa, and COT = 10. The retrieval yields CTP = 260 hPa, Δp = 60 hPa, and COT = 10.

Simulated OE retrieval results are shown in **Figs. 2.7–2.9**. Note that the *a priori* values were modified from the default values for these retrievals, given the placement of the simulated clouds. **Figure 2.7** shows a single layer ice cloud retrieval where the true cloud has COT = 10, CTP = 200 hPa, and Δp = 100 hPa. Here the *a priori* is assumed to be COT = 10, CTP = 400 hPa, and Δp = 50 hPa, and CER is assumed to be known without error. The retrieval converges after six iterations at the solution COT=10, CTP = 260 hPa, and Δp = 60 hPa.

Figure 2.8 shows a multi-layer cloud simulation having an identical ice cloud as in **Fig. 2.7** with the addition of a lower level liquid cloud at 850 hPa having COT = 10. Note that the retrieval still assumes a single-layer cloud in the forward model. As expected the retrieval converges on a solution that is well below the height of the higher cloud layer. These results highlight the sensitivity of these retrievals to presence of complex vertical cloud structures.

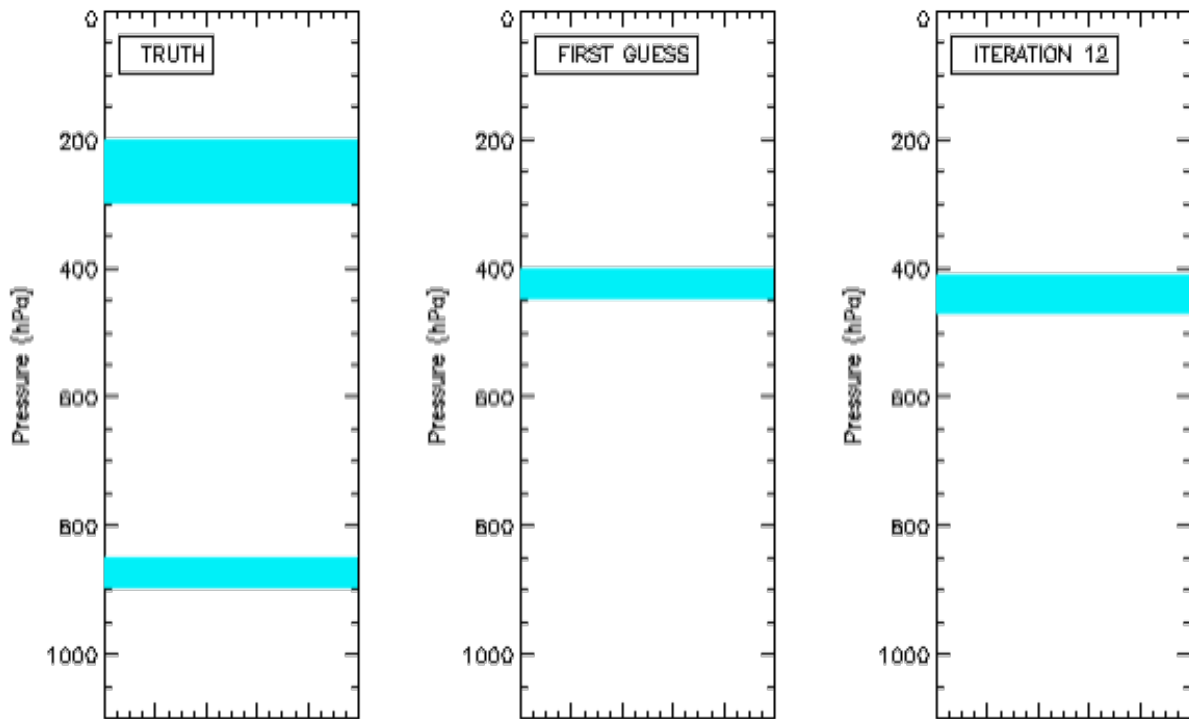


Figure 2.8. Same ice cloud as shown in Fig. 2.7 but with a lower-level liquid cloud with optical thickness of 10 inserted below. The single-layer retrieval assumption results in a retrieval solution below the higher cloud with optical thickness equal to the combined optical thickness of the two clouds.

Figure 2.9 shows the impact on retrieved CTP of the channels used in the OE retrieval. Here, individual reflectance ratios are turned off by setting their forward uncertainty to very high values so that they have no impact on the solution. In this retrieval, the simulated cloud has CTP = 600 hPa and COT = 10; the vertical dashed lines indicate the top and bottom of the cloud layer. The *a priori* value of CTP was 700 hPa. The retrievals were performed 50 times with each retrieval having observations perturbed by random noise within the 0.1 absolute reflectance error used in Fig. 2.6. Using only the 0.76/0.86- μm ratio (red distribution), the retrieval yields CTP just above 700 hPa, implying that a retrieval using only this ratio cannot improve much on the *a priori*, at least for this scenario. Including the 0.96/0.86- μm ratio that was shown to be sensitive to clouds in the middle troposphere greatly improves the accuracy of the retrieval, yielding CTP centered around 620 hPa (blue distribution). The accuracy is improved further with the addition of the 1.38/1.24- μm ratio (green distribution).

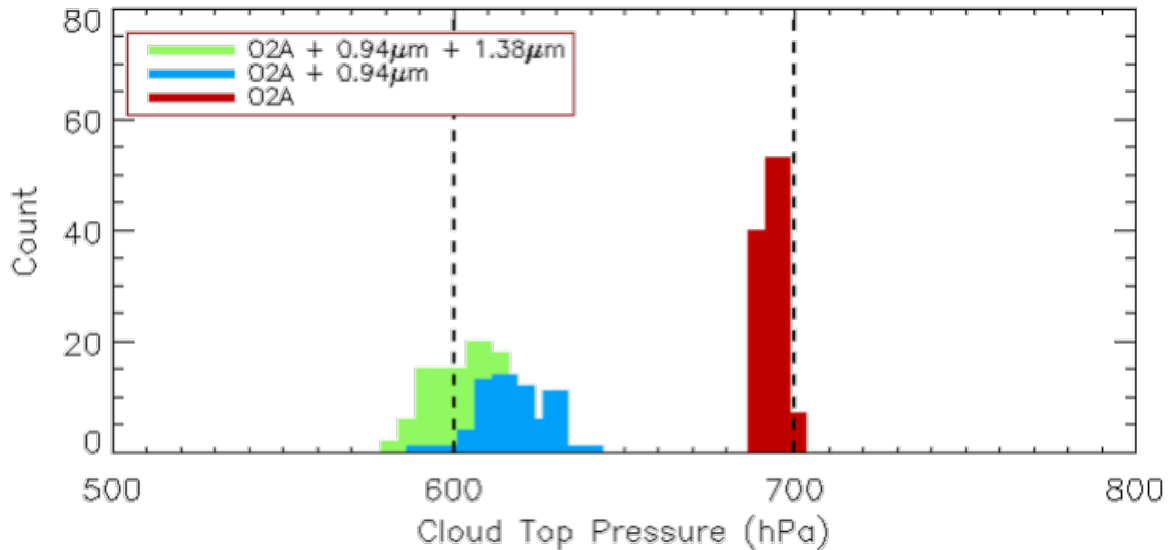


Figure 2.9. Simulated retrieval performance for a single-layer cloud with $COT = 10$ and $\Delta p = 100$ hPa. The true CTP is 600 hPa and the a priori value is 700 hPa.

The above OE retrieval simulations indicate the benefit in combining multiple gas absorption channels together for cloud top pressure and thickness retrievals. Further numerical simulations are needed to understand the likely uncertainties across a more extensive range of upper and/or lower cloud optical parameters using finalized OCI instrument requirements.

2.3. Cloud Thermodynamic Phase and Cloud Optical Properties from OCI

Existing operational cloud satellite algorithms, such as for MODIS and VIIRS, derive cloud thermodynamic phase from cloud observations in one or more discrete spectral channels where water absorbs solar and/or infrared radiation differently for liquid and ice phase. However, the measurement information often can be attributed to cloud optical properties of liquid or ice thermodynamic phase in an equally plausible way creating a challenge for passive cloud remote sensing. Therefore, a critical first step in useful cloud optical property retrievals is the retrieval of cloud thermodynamic phase. Incorrectly identifying cloud phase negatively impacts the interpretation of the effects of clouds on Earth’s climate.

The PACE Ocean Color Instrument (OCI) is notionally a hyperspectral imager from 350 nm to more than 800 nm with six discrete shortwave spectral channels (subset in **Table 2.1**) [PACE Science Definition Team, 2018]. Combinations of these channels also comprise subsets of the measurement channels used in cloud optical property retrievals from the MODIS and VIIRS instruments, where the significant difference in the subsets occurs in the 2- μ m window (i.e. the longest shortwave channel for MODIS is at 2135 nm, the longest shortwave channel for VIIRS is at 2250 nm, and the notional PACE OCI imager will have both 2135 and 2250 nm channels). Near 2 μ m, water strongly absorbs and retrievals of particle size have the greatest sensitivity.

In a theoretical study, we rigorously quantified the probability of liquid or ice phase and have demonstrated that PACE OCI, with two SWIR channels near 2 microns, provides more information on cloud thermodynamic phase than either MODIS or VIIRS can achieve with a single SWIR channel (and excluding infrared channels). We performed the study using a nonlinear statistical estimation approach called the

Generalized Nonlinear Retrieval Algorithm (GENRA) [Vukicevic et al., 2010] and the Collection 6 [Platnick et al., 2017] simulated cloud reflectance data used in the common MODIS/VIIRS Cloud Optical Properties product [Platnick et al., 2015] to represent simulated MODIS, VIIRS, and PACE OCI cloud reflectance measurements. GENRA is a tool based on the mathematical theory of general stochastic inverse problems (similar to Bayesian estimation theory). With GENRA, we quantify the distribution of retrieved parameters (phase, cloud optical thickness (COT) and particle effective radius (CER) based on knowledge from three sources of information: the measurements, a forward model that simulates our best understanding of the physics relating observations of cloud reflectance to the retrieved parameters, and any a priori information about the parameters that exists. A notable algorithm advancement necessary for the PACE OCI analysis required extending the GENRA technique to a binary thermodynamic phase space (i.e. liquid or ice) because previous cloud retrieval studies using GENRA assumed a cloud thermodynamic phase [Coddington et al., 2012].

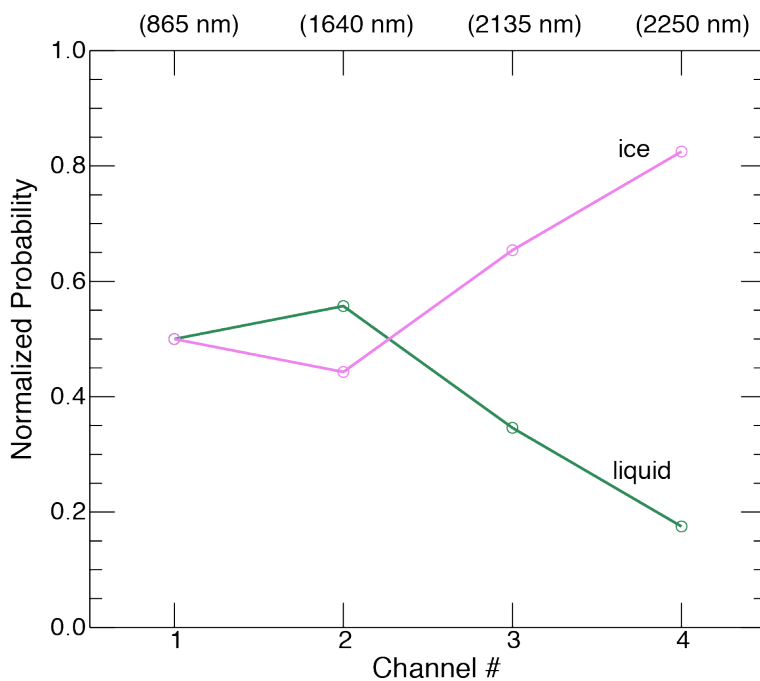


Figure 2.10. Cumulative probability for correctly discriminating ice cloud phase after ingesting information from a subset of the PACE OCI channel set combination (identified on top axis) into the GENRA algorithm for a “true” cloud type of COT=10, CER = 12 μm , and phase = ice.

Figure 2.10 shows the wavelength-dependent contributions to the cumulative probability of retrieving cloud thermodynamic phase for a thin (COT= 10) ice cloud with CER= 12 μm . The impact of two SWIR channels is highlighted by the increase in the probability of correctly identifying ice thermodynamic phase from approximately 65% at 2135 nm to approximately 85% for both 2135- and 2250-nm channels.

Cloud reflectance observations are dependent upon the properties of the cloud. Small differences in the absorption coefficient of liquid and ice water are increasingly larger in the SWIR relative to visible wavelengths such that as cloud particle size increases, the magnitude of cloud reflectance decreases. The extinction (absorption plus scattering) of radiation also depends upon particle size. Therefore, cloud retrieval algorithms utilize observations from measurement channels that are insensitive, or less sensitive, to water absorption to derive optical thickness and from those that are sensitive to water absorption to derive

particle effective radius. Therefore, the probability for which one COT, CER combination for a particular cloud phase can be uniquely identified from a COT, CER combination of the other cloud phase will vary over a broad range of COT and CER, and for different numbers and combinations of measurement channels.

Figure 2.11 shows results of the total probability in correctly retrieving ice phase given discrete, shortwave channels for MODIS (left), VIIRS (center), and PACE (right).

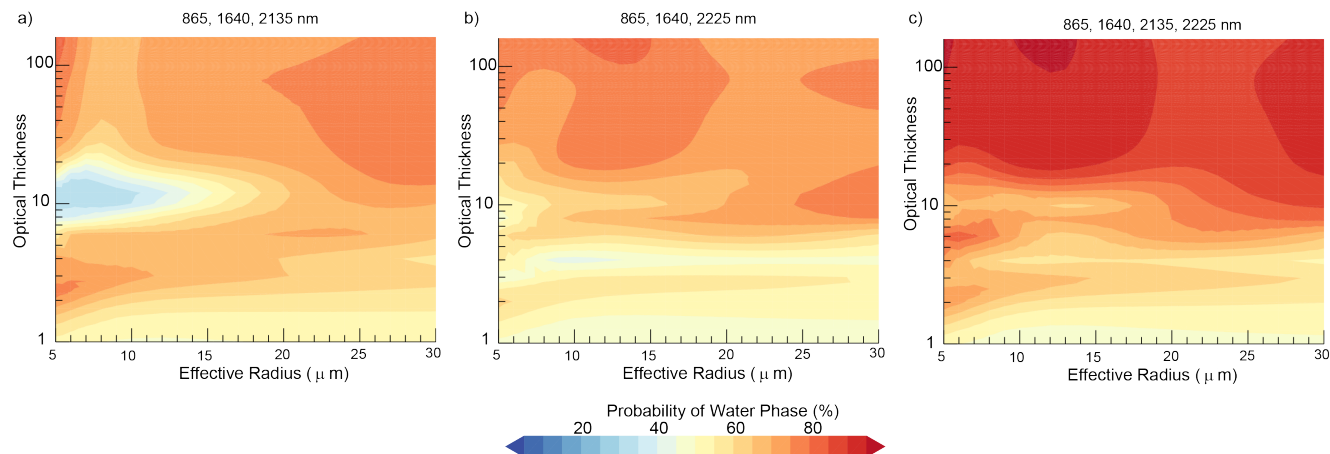


Figure 2.11. Contour plot of the percent probability of correctly retrieving liquid thermodynamic cloud phase from the parameter space jointly spanned by ice and liquid phase solutions when the “true” cloud phase is liquid. Values around 50% indicate an ambiguous phase retrieval (see text). The subplots are specific to specific measurement channel combinations: (a) three shortwave channels common to the MODIS imager, (b) three shortwave channels common to the VIIRS imager, and (c) four shortwave channels of the notional PACE OCI imager.

Figure 2.11 shows that the use of dual channels near 2 μm improves phase discrimination for regions of the cloud property parameter space where standard retrieval methods currently provide usable information (i.e. for moderate cloud optical thickness and larger particle sizes).

The results shown in **Figs. 2.10** and **2.11** assume a black surface because it is convenient to assess the ability for the PACE OCI to retrieve cloud thermodynamic phase (relative to MODIS and VIIRS) by establishing a baseline that has utility for simple, single-layer, cloud scenes over dark, ocean surfaces. However, the reality is that additional factors not considered above pose challenges for correctly retrieving cloud thermodynamic phase from PACE OCI. These factors are attributed to uncertainties in, and unaccounted for natural variability of, non-retrieved forward model inputs (i.e. prescribed surface reflectance, atmospheric state) and forward model assumptions such as plane-parallel clouds that do not reflect true atmospheric conditions where radiation from clouds may enter/exit from the edges of clouds or have passed through multiple layers of clouds, of potentially differing thermodynamic phase in different layers.

The reflected radiation from clouds is influenced by the surface and atmospheric below the cloud, particularly for thin clouds. We used the GENRA tool to quantify the probability of retrieving the correct thermodynamic phase for clouds above forested regions, deserts, and bright snow surfaces where a representative albedo (see **Fig. 2.12**) of these surfaces was obtained from gap-filled MODIS surface spectral albedo datasets [Schaaf *et al.* 2011] from March 2005 (MYD08_D3.A2005091.hdf). The contributions of the non-zero Lambertian surfaces to the MODIS, VIIRS, and PACE cloud reflectances were added using the MOD06 adding-doubling approach [King *et al.* 1987]. **Figure 2.13** illustrates a decrease in the probability for correctly retrieving liquid water thermodynamic phase above a bright, snow surface,

particularly for clouds with optical thickness values < 10 while thicker clouds are relatively unaffected by the underlying surface.

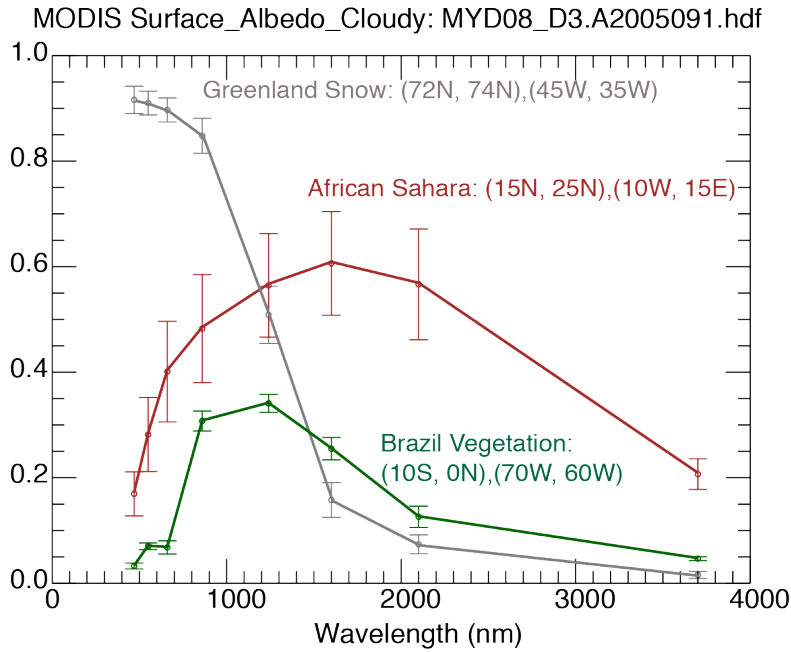


Figure 2.12. MODIS surface albedos obtained from representative locations of snow surface (Greenland), desert (African Sahara), and forest vegetation (Brazil). The error bars signify the standard deviation of the surface albedo over the representative region selected (indicated as longitude, latitude ranges in the legend).

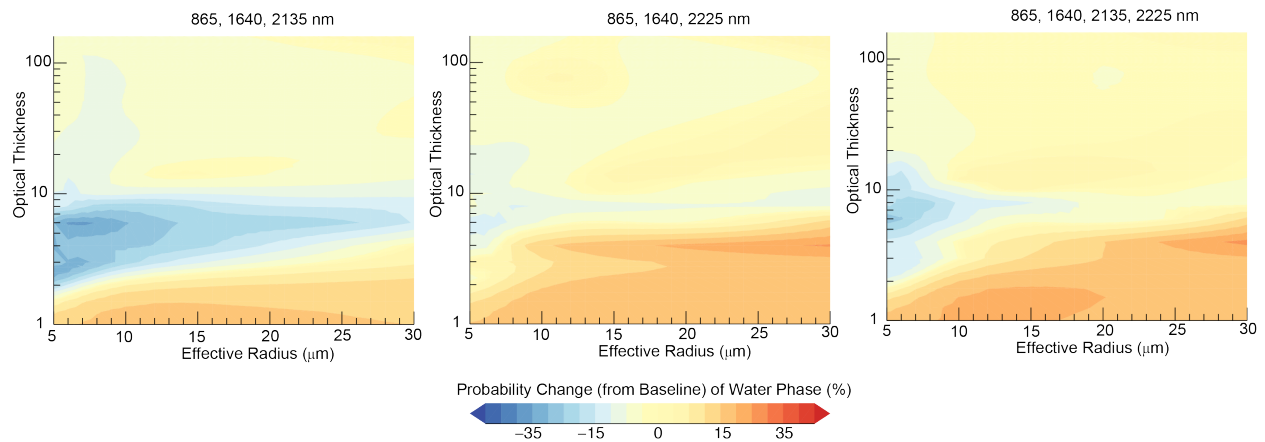


Figure 2.13. Change in probability of liquid water phase discrimination for cloud retrievals above a bright snow surface (“Greenland Snow” in Fig. 2.12) relative to a “baseline”, uniformly dark surface type. Blue values indicate reductions in probability of phase detection. Yellow values indicate cloud property types where the probability of liquid phase discrimination is not affected by changes in surface reflectance.

Thus far, we’ve focused primarily on shortwave-only cloud thermodynamic phase retrievals with MODIS, VIIRS, and the PACE OCI imagers. However, the GENRA tool also provides probability distributions that characterize cloud optical thickness and droplet effective radius retrievals as a function of uncertainties in the measurements and the uncertainties in the simulated cloud reflectances from the forward model. We chose to investigate the impacts of surface albedo on cloud retrievals because the

surface albedo is a necessary input to algorithms for the retrieval of cloud optical properties and it is subject to its own set of uncertainties. A comparison of surface albedo retrieved from an airborne radiometer over approximately 400 km miles above a region of soil and dead vegetation that was coincident with a MODIS satellite overpass suggested differences between aircraft and satellite surface albedos on the order of ± 0.025 (albedo units) [Coddington et al. 2008].

We performed a theoretical study that investigated the impact of a $+0.025$ bias in snow surface albedo on retrieved cloud optical properties for the PACE OCI. This degree of systematic error in the retrieved surface albedo primarily impacted (biased high) simulated cloud reflectance, particularly at shorter wavelengths (not shown). Using GENRA, we obtained the corresponding maximum likelihood solution in COT and CER that reflects the parameter values for the best fit between observed and simulated cloud reflectance for two cases: one with a systematic high bias in the retrieved snow surface albedo, and the other without a bias. The results are shown in **Fig. 2.14**, where the retrieved cloud optical thickness affected by the biased surface albedo retrieved optical thickness is two units smaller than the retrieval not affected by the bias. For this case, no impact on effective radius was determined. The basis for the subsequent bias in the cloud properties can be interpreted by the following. The systematic high bias in the retrieved surface albedo has propagated into a high bias in simulated cloud reflectance (particularly at shorter wavelengths) such that the measured cloud reflectance (i.e. the “truth”) is a best-fit match to the simulated cloud reflectance for a thinner cloud of the same effective radius.

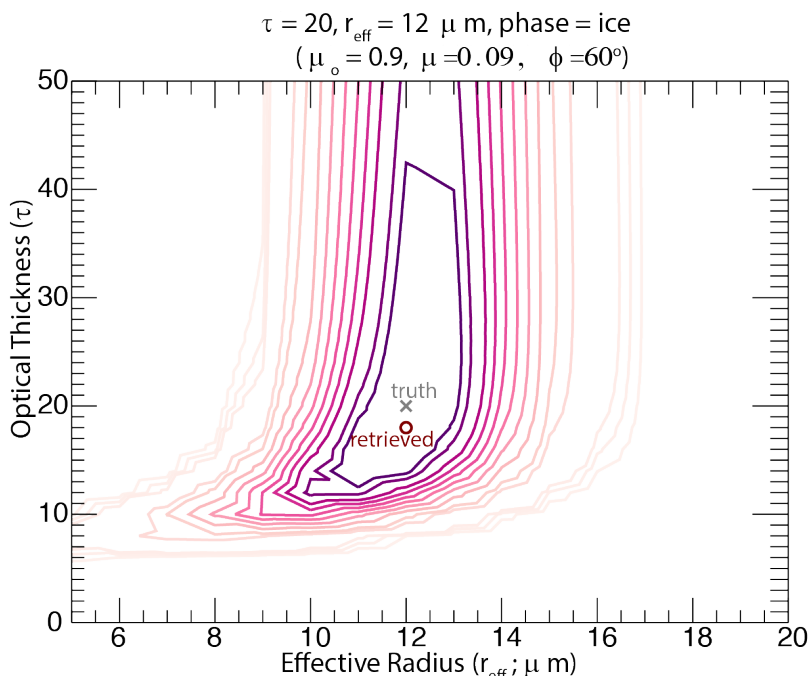


Figure 2.14. The 2-dimensional contour plot of optical thickness and particle effective radius for a true cloud type of (COT=20; CER= 10 μm ; phase=ice) obtained with the GENRA algorithm after sequentially incorporating cloud reflectance observations over a bright snow surface at four PACE shortwave retrieval wavelengths. The “o” indicating the retrieved cloud property pair is respective of a case where a systematic high bias in retrieved snow surface albedo (a necessary, ancillary input parameter for cloud optical property retrievals) has propagated into the cloud retrieval such that the cloud optical thickness value retrieved is two units smaller than a retrieval performed under the same conditions except the retrieved snow surface albedo did not have a high bias.

In summary, we find the PACE OCI improves the probability of discriminating the correct cloud thermodynamic phase relative to shortwave-only retrievals from MODIS or VIIRS, for regions of the cloud

property parameter space where standard passive cloud retrieval methods currently provide usable information (i.e. for moderate cloud optical thickness values and larger particle sizes). Retrievals of cloud optical thickness and droplet effective radius from PACE OCI, like other current and heritage imagers, are impacted by uncertainties in, and natural variability of, non-retrieved forward model parameters such as column water vapor and surface albedo that are not accounted for correctly during the retrieval process. It is an ongoing process to understand, and account for, the impacts of these uncertainties for improving the utility of MODIS, VIIRS, and PACE OCI cloud products for climate studies.

The above phase study used the MODIS Collection 6 (C6) ice and liquid particle optical models [Platnick *et al.* 2017]. For the ice phase, the retrievals require assumptions for the particle habit and distributions. Comparisons of forward RT calculations with satellite remote sensing using polarization of reflected sunlight from POLDER suggest that ice crystals with roughened surfaces significantly outperform smooth ice crystals [e.g., Cole *et al.* 2014; Hioki *et al.* 2016], and similarly for airborne Research Scanning Polarimeter (RSP) observations [van Diedenhoven *et al.* 2013] (also see Sect. 3.2). Moreover, reflectance-based COT retrievals using a single habit, namely, severely roughened compact aggregates composed of eight solid columns [Yang *et al.* 2013], were found to provide closure with thermal IR-based retrievals and are in better agreement with cloud-aerosol lidar with orthogonal polarization (CALIOP) v4 cirrus optical thickness retrievals [Holz *et al.* 2015]. Based on these studies, the MODIS C6 ice models use a gamma particle size distribution (effective variance 0.1) consisting of the Yang *et al.* severely roughened aggregated columns.

2.4. Cloud Spatial Resolution Sensitivities with OCI

Background: Spatial resolution is an important instrument parameter for OCI that can have a particularly significant impact on cloud optical and microphysical property retrievals. Clouds have highly variable horizontal structures spanning from the mesoscale (~100 km) down to scales that cannot be resolved by most current satellite sensors (e.g., sub-pixel scale <100 m) [Cahalan and Joseph, 1989; Wood *et al.*, 2008]. The fine spatial structures of clouds pose several challenges for satellite cloud remote sensing. First, it is inevitable that some cloudy pixels identified by a masking algorithm are partly cloudy. Simply flagging these pixels (the strategy adopted in MODIS Collection 6 (C6)) and eliminating the population from statistical calculations could lead to significant sampling bias. Alternately, including these pixels in the product's statistical calculations would likely result in a large amount of retrievals with high uncertainty and potential biases due to surface contamination. Indeed, our recent analysis of C6 MOD06 product reveals that the retrieval failure rate for partly cloudy pixels is much higher than overcast pixels [Cho *et al.* 2015]. Secondly, even if a cloudy pixel is overcast, there could still be significant sub-pixel level cloud heterogeneity. Most operational remote sensing algorithms are based on the plane-parallel homogenous pixel assumption. The deviation of real-world cloud from this assumption can lead to significant biases in COT and CER retrievals, known as the plane-parallel homogenous bias (PPHB) [Marshak *et al.*, 2006; Zhang and Platnick 2011; Zhang *et al.* 2016]. Last, cloud horizontal structure can lead to the so-called three-dimensional radiative effects, such as radiative smoothing and illuminating/shadowing effects [Marshak *et al.*, 2006, Davis and Marshak 2010]. These effects currently cannot be accounted for in radiative transfer-based retrieval algorithms, leading to significant instantaneous (pixel-level) uncertainties and potentially aggregated (Level-3) uncertainties in the retrieval product.

The abovementioned issues caused by cloud heterogeneity have a strong dependence on the spatial resolution of the instrument. The baseline OCI design has a notional spatial resolution of 1km. The science definition team also recommended several other concepts to meet the requirements for addressing different

scientific questions [PACE Science Definition Team, 2018]. Here we report our studies on the capability and limitations of these concepts for remote sensing of the liquid-phase cloud τ and r_e .

Theoretical advances: We developed a framework based on the 2-D Taylor expansion for quantifying the impacts of sub-pixel reflectance variance and covariance on COT and CER retrievals based on the bi-spectral method. Retrievals of COT (τ) and CER (r_e) are not exclusively orthogonal throughout the solution space and therefore cannot be assumed to be independent and considered separately when investigating the impact of sub-pixel cloud reflectance variations on the bi-spectral method. In the framework of Zhang *et al.* [2016], we use a second-order Taylor expansion of a two-variable function to understand and quantify the impacts of sub-pixel variances of VIS/NIR and SWIR cloud reflectances and their covariance on the retrievals. **Eq. 2.1** below is the basic equation of this framework. Note that MOD06 pixel-level retrieval uncertainty calculations [Platnick *et al.*, 2017] use the same formulation, though only include the first-order expansion term.

$$\underbrace{\begin{pmatrix} \Delta\tau \\ \Delta r_e \end{pmatrix}}_{\text{retrieval bias}} = \underbrace{\begin{pmatrix} \frac{1}{2} \frac{\partial^2 \tau(R_{\text{VIS}}, R_{\text{SWIR}})}{\partial R_{\text{VIS}}^2} & \frac{\partial^2 \tau(R_{\text{VIS}}, R_{\text{SWIR}})}{\partial R_{\text{VIS}} \partial R_{\text{SWIR}}} & \frac{1}{2} \frac{\partial^2 \tau(R_{\text{VIS}}, R_{\text{SWIR}})}{\partial R_{\text{SWIR}}^2} \\ \frac{1}{2} \frac{\partial^2 r_e(R_{\text{VIS}}, R_{\text{SWIR}})}{\partial R_{\text{VIS}}^2} & \frac{\partial^2 r_e(R_{\text{VIS}}, R_{\text{SWIR}})}{\partial R_{\text{VIS}} \partial R_{\text{SWIR}}} & \frac{1}{2} \frac{\partial^2 r_e(R_{\text{VIS}}, R_{\text{SWIR}})}{\partial R_{\text{SWIR}}^2} \end{pmatrix}}_{\text{matrix of 2nd derivatives}} \underbrace{\begin{pmatrix} \sigma_{\text{VIS}}^2 \\ \text{COV} \\ \sigma_{\text{SWIR}}^2 \end{pmatrix}}_{\text{heterogeneity vector}} \quad \text{Eq. (2.1)}$$

The novelty of this framework is to decomposes the retrieval bias (i.e. LHS see Platnick *et al.*, 2017) due to sub-pixel cloud reflectance variability into two parts: 1) the magnitude of the sub-pixel reflectance variance and covariance specified by second term on the RHS of **Eq. 2.1**, and 2) the matrix of the second-order derivatives of the LUT with respect to VIS/NIR (R_{VIS}) and SWIR (R_{SWIR}) reflectances (referred to as “2nd derivative matrix” elements). Given the LUT, the matrix of 2nd derivatives can be easily derived from straightforward numerical differentiation. An example of matrix element based on the LUT for 0.86- μm and 2.1- μm reflectances is shown in **Fig. 2.15**.

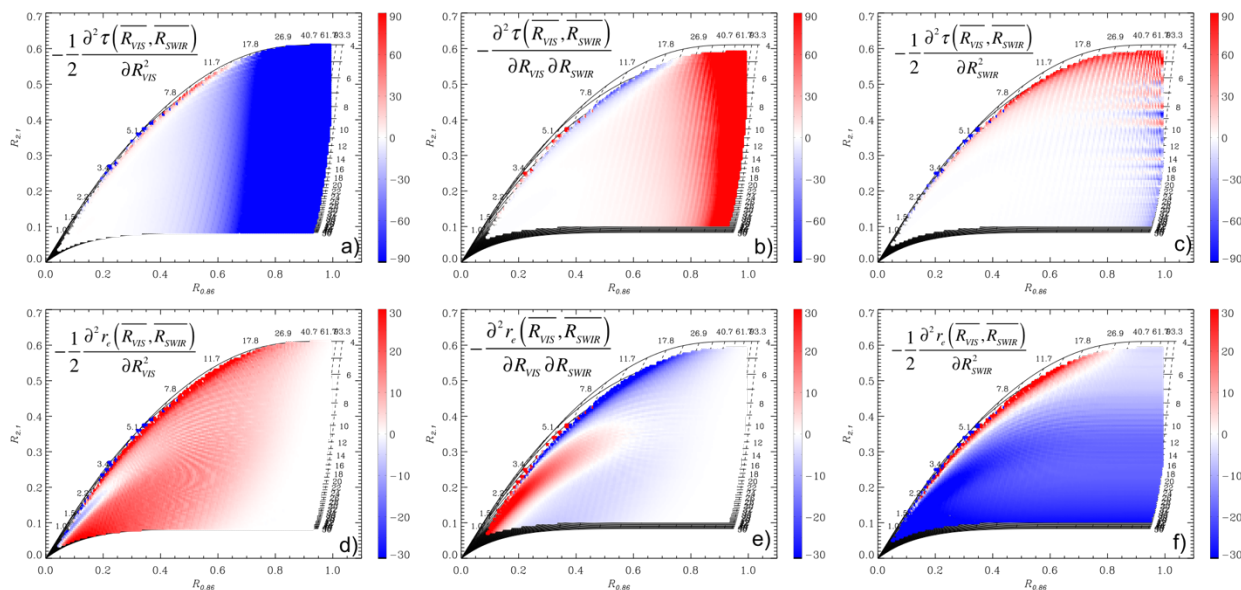


Figure 2.15. The sign and magnitude of each 2nd derivative term in Eq.2.1 derived from the 0.86 μm and R2.1 LUT.

It is clear from **Eq. 2.1** that the retrievals are not only influenced by the sub-pixel variation of the primary band (i.e., R_{VIS} for COT and R_{SWIR} for CER) but also by the variation of the secondary band (i.e., R_{VIS} for CER), as well as the covariance of the two bands. Therefore, it reconciles and unifies the theoretical frameworks in *Marshak et al.* [2006], *Zhang and Platnick* [2011] and *Zhang et al.* [2012]. In particular, the impact of the PPHB on COT and CER described in *Marshak et al.* [2006], corresponds to the upper-left and lower-right terms (2nd derivative elements), respectively. As shown in **Fig. 2.15** both terms are generally negative over the most part of LUT, consistent with the finding of *Marshak et al.* [2006] that ignoring sub-pixel variability tends to result in an underestimation of the pixel average of the retrieved quantity if COT and CER retrievals are considered separately and independently (i.e., negative $\Delta\tau$ and Δr_e). On the other hand, $\Delta\tau$ and Δr_e are also influenced by other terms in the matrix. Physically, these terms arise from the fact that both R_{VIS} and R_{SWIR} are not orthogonal to COT and CER.

The theoretical framework described above offers a comprehensive explanation for the root of PPHBs in cloud optical retrievals. It also provides qualitative guidance for understanding the trade-off between different spatial resolutions of OCI recommended by the SDT. *In general, an increase of spatial resolution can help reduce the PPHB, i.e., underestimation of COT and overestimation of CER.*

Numerical test beds: We also developed two types of numerical test beds for quantitative investigation of the impacts of different OCI spatial resolutions on cloud property retrievals quantitatively. The first one described below is based on the high-resolution (30 m) cloud retrievals from the Advanced Spaceborne Thermal Emission and Reflection Radiometer (ASTER) instrument onboard of Terra [*Werner et al.* 2016]. The other one that will be described in Chapter 3 is based on cloud fields from a Large-eddy Simulation (LES) model. ASTER is an imaging spectroradiometer aboard the NASA Terra satellite. ASTER collects data in 15 spectral bands, covering the visible to the thermal IR spectral wavelength range. The spatial resolution of an individual ASTER pixel in the visible to near-infrared spectral wavelength range (VNIR) is 15 m, while it is 30 and 90 m in the shortwave-infrared (SWIR) and IR spectral wavelength range, respectively. Recently [*Werner et al.* 2016], we have implemented MOD06-like COT and CER retrievals from ASTER 0.86 and 2.1 μm bands using CHIMAERA (Cross-platform HIGH resolution Multi-instrument AtmosphERIC Retrieval Algorithms) that is the backbone of the operational MODIS cloud retrieval algorithm.

The high-spatial resolution of ASTER allows us to compare cloud property retrievals at the notional OCI spatial resolution ~ 1 km with retrievals at a native 30 m resolution. We selected about 100 marine-boundary-layer cloud scenes of the coast of California for this analysis (**Fig. 2.16**). An example is shown below.

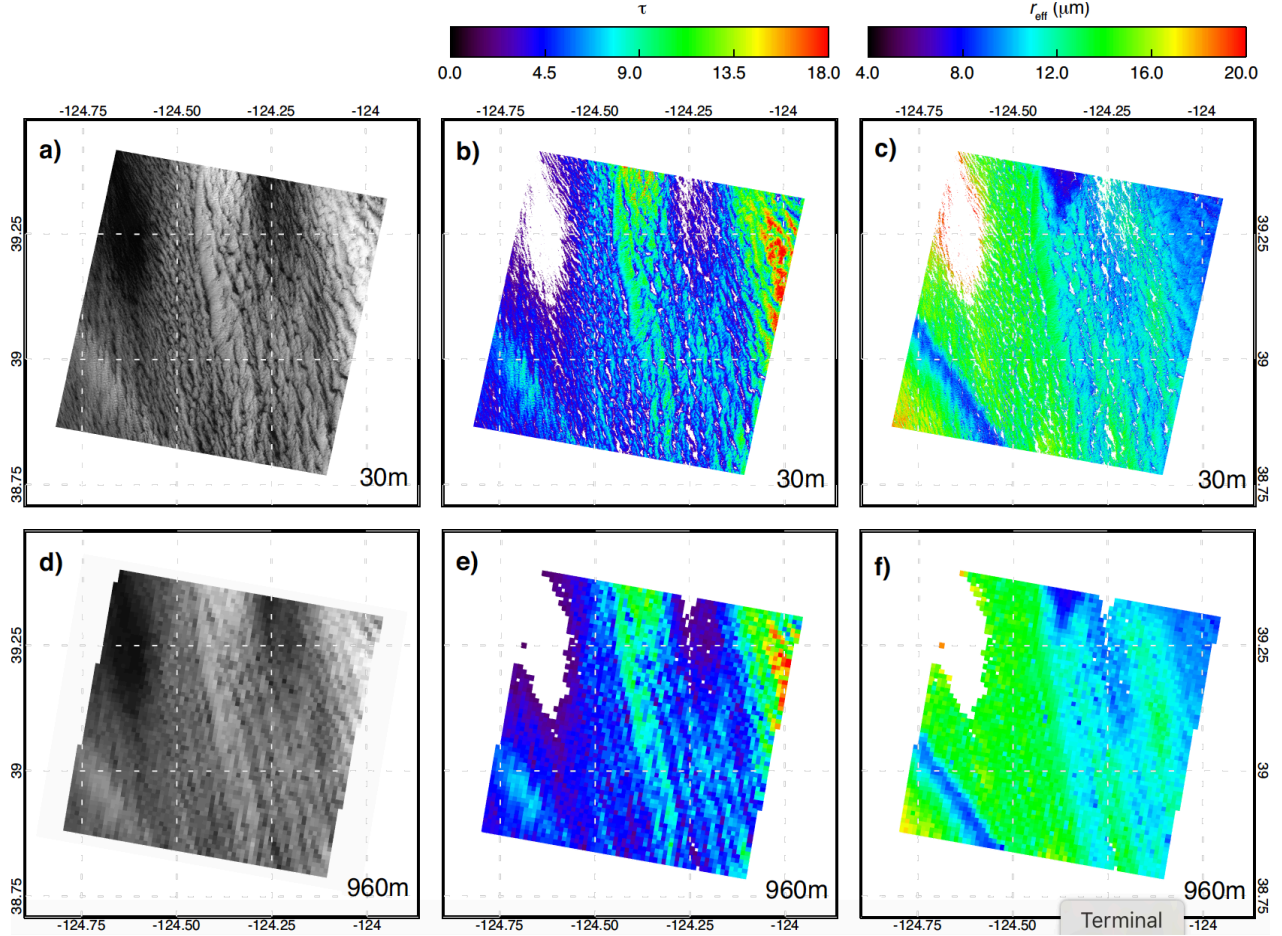


Figure 2.16. An ASTER cloud scene sampled on December 16, 2004 off the Coast of California. Upper panel shows the cloud reflectance in the 0.86- μm band (a), cloud COT (τ) (b) and CER (r_e) (c) retrievals at the 30-m resolution. Lower panel shows the corresponding plots at the notional OCI resolution ~ 1 km.

Maps of the observed $\Delta\tau$ and Δr_e for this example from numerical simulation are provided in **Figs. 2.17(a)** and **2.17(d)**, respectively. Here, the mean values $\overline{\tau}(R_{VNIR}, R_{SWIR})$ and $\overline{r_e}(R_{VNIR}, R_{SWIR})$ are calculated from the high-resolution retrievals based on 30 m ASTER observations, while $\tau(R_{VNIR}, R_{SWIR})$ and $r_e(R_{VNIR}, R_{SWIR})$ are the retrievals based on aggregated reflectances at 960 m (i.e., OCI baseline resolution). Because clear sky pixels have no defined CER (whereas these samples can be defined to exhibit COT=0), the PPHB is only calculated for pixels with a sub-pixel cloud cover of $C_{\text{sub}} = 1.0$. Pixels with $C_{\text{sub}} < 1.0$ are shown in grey colors and are not included in the analysis. For this scene $\Delta\tau$ and Δr_{eff} are exclusively negative and positive, respectively, with $-0.4 < \Delta\tau < 0$ and $0 \mu\text{m} < \Delta r_{\text{eff}} < 0.6 \mu\text{m}$. The largest $\Delta\tau$ are observed for pixels containing thick clouds, while the thin cloud regions exhibit the largest Δr_{eff} . The predicted PPHB results, predicted by our framework are shown in **Fig. 2.17(b)** for $\Delta\tau$ and **Fig. 2.17(e)** for Δr_{eff} . It is obvious that both the sign and magnitude of the predicted PPHB results agree well with observed values shown in **Figs. 2.17(a)** and **(d)**. A pixel-level comparison between the predicted and true PPHB is shown in **Figs. 2.17(c)** and **(f)** for $\Delta\tau$ and Δr_{eff} , respectively. Colors indicate the pixel value of the inhomogeneity index $H_{\sigma_{VIS}}$. Several interesting observations can be made from these scatter plots. First, the objectively good agreement between predicted and numerical PPHB seen in the maps in is confirmed, with data points close to the 1:1 line and high values of Pearson's product-moment correlation coefficient of $r \geq 0.86$. For $\Delta\tau$ there seems to be no dependence on $H_{\sigma_{VIS}}$, however, there is an increase of

Δr_{eff} with an increase in $H_{\sigma_{\text{VIS}}}$. Overall, the prediction works better for $\Delta\tau$ than for $\Delta\tau$ and Δr_{eff} , which can be attributed to the more complex distribution of the matrix elements (see also *Zhang et al. [2016]*).

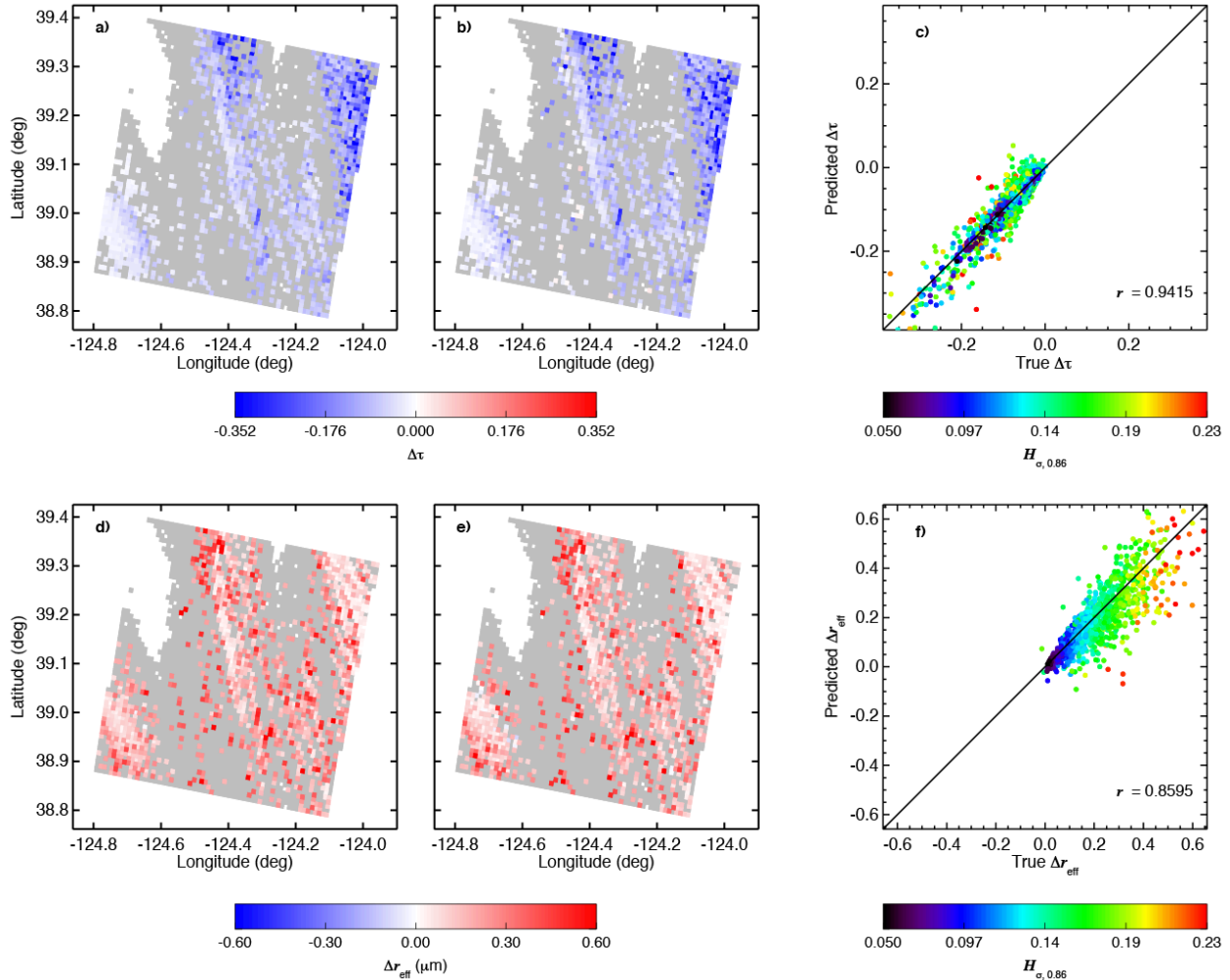


Figure 2.17. (a) Observed and (b) predicted change in COT ($\Delta\tau$) for the ASTER cloud scene sampled on December 16, 2004 off the Coast of California. (c) Scatter plot of observed versus predicted $\Delta\tau$. (d)–(f) Same as (a)–(c) but for the change in CER (Δr_{eff}).

The results presented in **Fig. 2.16**, which is assuming a notional baseline OCI resolution of 1 km (actually 960 m), confirm that (1) similar to the MODIS operational retrieval (also at 1 km) sub-pixel cloud heterogeneity is likely to cause underestimation of COT and overestimation of CER in the OCI cloud product; and (2) our theoretical frame work can be used to estimate the magnitude of these biases *if a sensor is available with high enough spatial resolution to estimate the reflectance variances within the larger pixel FOV*.

Therefore, to take our trade-off studies one step further, one possible design of the OCI is to offer relative high-spatial resolution only at selected spectral bands (e.g., 0.86 μm), as discussed in the PACE SDT report [*PACE Science Definition Team, 2018*]. In the analysis shown in **Fig. 2.17**, we evaluate the feasibility of using a single high-resolution reflectance band in the VNIR to estimate the impacts of PPHB on COT and CER retrievals. As shown in the figure below (**Fig. 2.18**), our framework provides reasonable estimate of the PPHB bias in both COT and CER retrievals even if there is only a single high-resolution band in the VIS spectral.

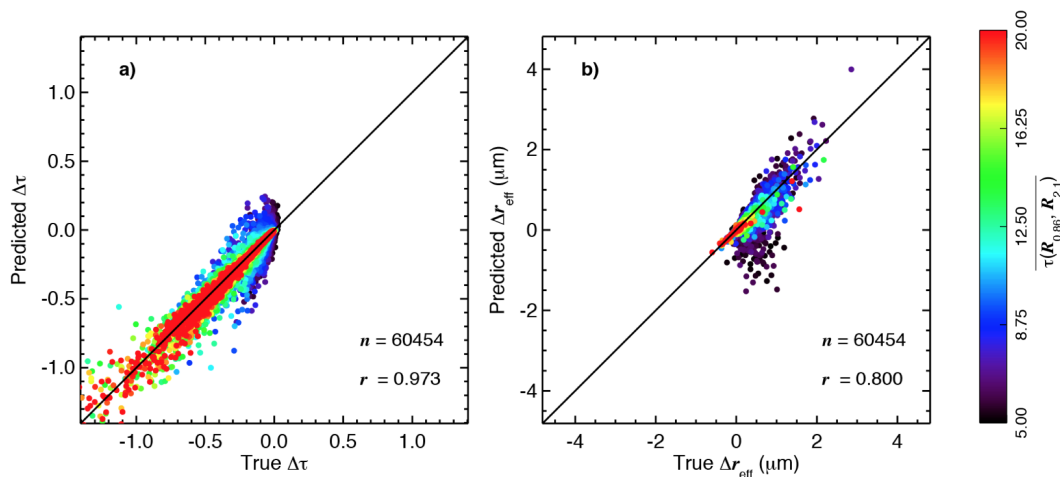


Figure 2.18. PPHB bias in COT (τ) (a) and CER (r_e) (b) retrieval predicted using a single high-resolution VIS band in comparison with numerical results.

Summary: At a notional $\sim 1\text{km}$ spatial resolution, the OCI bi-spectral cloud property retrieval is facing the same challenges caused by cloud heterogeneity, as many current satellite instruments such as MODIS and VIIRS. We have recently developed a theoretical framework that can provide a comprehensive and quantitative estimate of the impacts of sub-pixel level cloud heterogeneity on both COT and CER retrievals *if selected higher spatial resolution OCI band(s) are available*. In addition, we also developed test bed based on the high-resolution ASTER observations to study the trade-off between different design concepts of OCI. *Our study indicates that even a single high-spatial resolution band ($\sim 100\text{ m}$) in the non-absorbing spectral region (e.g., 0.86 and $0.64\ \mu\text{m}$) can significantly help estimate and reduce the uncertainties caused by cloud heterogeneity using our theoretical framework.*

3. Cloud Properties from a Notional PACE Polarimeter

PACE will attempt to fly a multiple spectral, multi-angular polarimeter for atmospheric correction, as well as for producing aerosol and cloud property products. While the detailed instrument characteristics for the PACE polarimeter are still to be determined, we note the SDT report used a baseline concept similar to the operational 3MI (Multi-viewing Multi-channel Multi-polarization Imaging instrument) instrument being developed by ESA/EUMETSAT. We have made a similar baseline assumption in the discussion that follows, including the specific expectations that a PACE polarimeter will measure the total radiance and linear polarization (i.e., I, Q and U of Stokes Vector) of reflected sunlight at a minimum of one non-absorptive cloud band (e.g., 0.86 μm) with a spatial resolution no better than OCI and an angular resolution fine enough to resolve the primary and supernumerary cloud bows. Again, the extent to which this is realizable remains to be determined by the PACE project.

3.1. Liquid Water Cloud Polarimetric Retrievals

In this section, we report our study of the advantages and limitations of liquid water cloud microphysical retrievals based on the above polarimeter assumptions in comparison with the spectral-based total reflectance retrievals from OCI.

Basics of polarimetric water cloud retrievals: For the remote sensing of the microphysical properties of liquid phase clouds, the PACE polarimeter can lever the POLDER and Research Scanning Polarimeter algorithms (e.g., *Bréon and Goloub [1998]* and *Bréon and Doutriaux-Boucher [2005]* and *Alexandrov et al. [2012]*). These algorithms retrieve the cloud effective radius (CER) and effective variance (v_e or CEV) of the droplet size distribution near the optical top of the cloud. The information for these retrievals come from the angular pattern of polarized cloud reflectance in the cloud bow. Because multiple scattering tends to reduce the degree of polarization, polarized cloud reflectance primarily consists of single scattered radiation. As such, the angular pattern of the polarized cloud reflectance is closely related to the pattern of phase matrix element P_{12} with respect to scattering angle. **Figure 3.1** shows the P_{12} at 0.86 μm for a variety of cloud droplet size distributions with different CER and CEV. All P_{12} have a prominent peak around 140° known as the primary cloud bow. The so-called supernumerary bow is the peak located at larger scattering angles between 150° and 160° . For a fixed CEV (e.g., 0.02 in **Fig. 3.1a**), the peak of supernumerary bow gradually shifts to a smaller scattering angle (i.e., closer to the primary bow) as CER increases. For a fixed CER (e.g., 10 μm in **Fig. 3.1b**), the peak of supernumerary bow is gradually reduced as CER increases. These variations of P_{12} provide the information content for retrieving liquid cloud microphysics from a PACE polarimeter. Algorithms such as described by *Alexandrov et al. [2012]* use the relative structure of the polarized reflectances to retrieve droplet size information, while fitting additional auxiliary functions that remove smooth angular variations and angular shifts from the data. This makes the retrievals especially robust against 3D-radiative transfer biases, mixed-phase conditions and overlying cirrus or aerosols [*Alexandrov et al. 2012*].

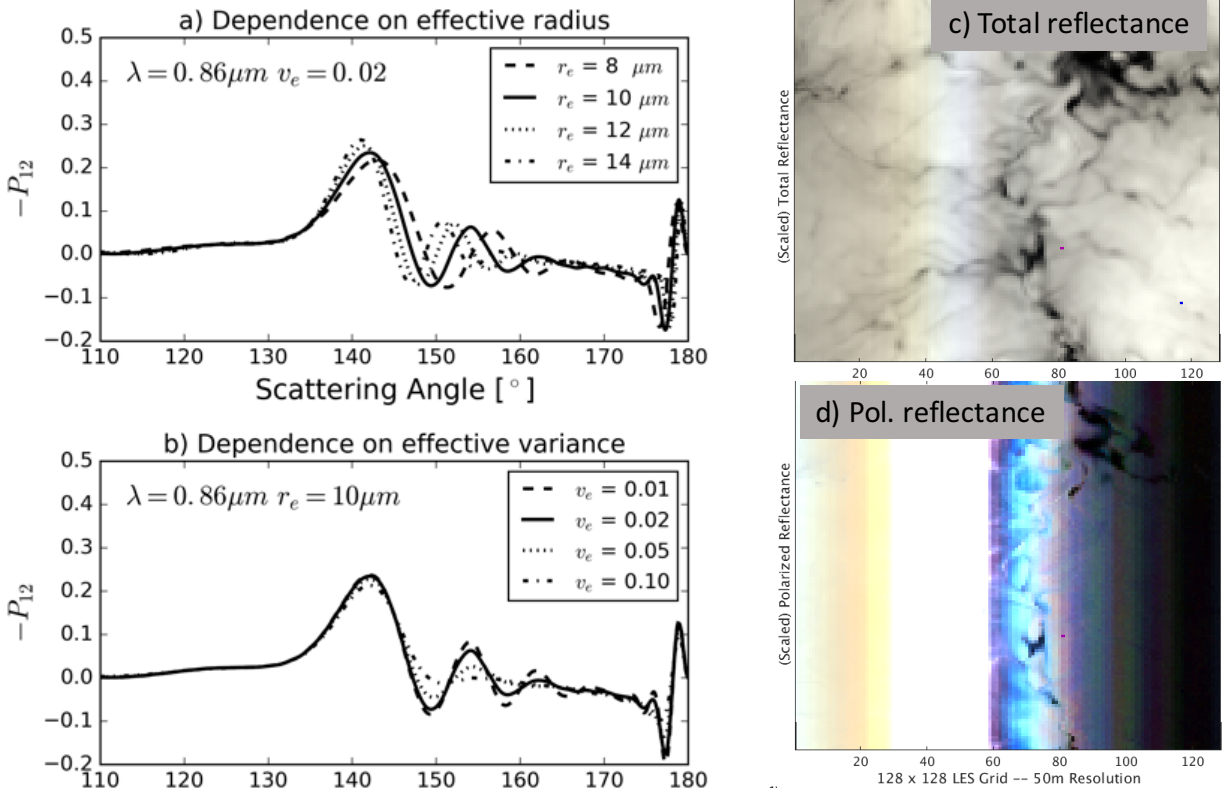


Figure 3.1. The phase function element P_{12} as a function of scattering angle for cloud droplets size distributions with different (a) CER (r_e) and (b) CEV (v_e). Synthetic RGB images ($R=0.86 \mu\text{m}$, $G=0.64 \mu\text{m}$ and $B=0.47 \mu\text{m}$) based on (c) total and (d) polarized cloud reflectance simulated from our PACE polarimeter cloud observation simulator for a LES cloud field with a solar zenith angle of 20° .

LES-based PACE cloud observation simulator: To facilitate our study, we developed a numerical simulator to represent the multi-spectral, multi-angular cloud reflectances available from a notional PACE polarimeter. The simulator uses simulated 3-D cloud fields with detailed bin microphysics from a large-eddy simulation model [Ackerman et al. 2004] as input. It uses the polarized radiative transfer models, e.g., polarized adding doubling code [de Haan et al. 1987] and the 3D Monte-Carlo Polarized radiative transfer code (3DMCPOL) [Cornet et al. 2010], to simulate the total and polarized cloud reflectance for the input LES cloud field. An example from our simulator is given in **Fig. 3.1**. The LES cloud field is simulated using the meteorological conditions from the DYCOM-II field campaign. The total and polarized cloud reflectances for this LES cloud fields are simulated at the following three wavelengths: 0.86, 0.64 and 0.47 μm used respectively for the R, G, B composite shown in the figure. The solar zenith angle is set to 20° . For each pixel, cloud reflectances are simulated for a total of 150 viewing geometries with viewing zenith ranging from $\pm 60^\circ$ to mimic multi-angular observations from a notional polarimeter. **Figures. 3.1c** and **3.1d** show the synthetic RGB images for this case based on the total and polarized reflectance, respectively.

In addition to polarization simulations at the three cloud non-absorption bands mentioned in the previous paragraph, we also simulate cloud reflectances at two bands with significant absorption, i.e., 2.1 μm and 3.7 μm that can be used to simulate total reflectance cloud property retrievals from OCI.

Advantages: Using the above described PACE cloud observation simulator, we compared the cloud r_e retrievals based on polarimetric (i.e., PACE polarimeter) method with those based on bi-spectral (i.e.,

PACE OCI) method for three LES cases. The comparison results are summarized in **Fig. 3.2**. A pixel-to-pixel comparison at the LES resolution (**Fig. 3.2a**) reveals above all that the reff retrievals from the two retrievals are in excellent agreement ($R > 0.95$). However, some outliers marked by the red circle are worth noting. For these pixels, the polarimetric method tends to retrieve a small value around $2\sim 7\mu\text{m}$ for r_e , while the r_e retrievals from the spectral method are substantially larger, varying from $5\mu\text{m}$ up to $30\mu\text{m}$. An examination of LES field indicates that these pixels tend to be optically thin, most with $\tau < 3$. After a further analysis of the location of these points in the Nakajima-King look-up library (LUT), we found that they are in the so-called “multiple solution domain” of bi-spectral LUT. In the bi-spectral method, given a pair of observed VIS and SWIR cloud reflectances, there is usually only one possible combination of COT and CER in the LUT that can generate such observation (i.e., single solution). However, in the multiple solution domain of the LUT, there exist more than one possible combinations of COT and CER that could generate the observed VIS and SWIR cloud reflectances (i.e., a multiple solution). Following the MODIS operational retrieval algorithm, we reported the solution with larger CER when the pixel is in the multiple solution space. This is an inherent limitation of the bi-spectral method for cloud microphysics retrieval. The CER retrieval based on the polarimetric method does not have such limitations. This explains why the bi-spectral retrievals tend to be larger than the polarimetric values for these pixels.

As discussed in *Sect. 2.4*, sub-pixel cloud heterogeneity can cause significant PPHB in cloud property retrievals based on the bi-spectral method. We also investigated the sensitivity of the polarimetric method to spatial resolution. First, we progressively aggregated the simulated polarized reflectance from 50m to several coarser resolutions, e.g., 100 m, 200 m, 400 m and 1 km. Then CER retrievals based on both polarimetric and bi-spectral methods are made and compared at each resolution. Such experiment is made for all LES scenes, but for the sake of clarity only results from the ATEX case are shown in **Fig. 3.2b**. In the figure, each data point corresponds to a LES pixel with the size of the symbol indicating the spatial resolution (e.g., 100 m, 200 m, 400 m and 800 m) and the color indicating the sub-pixel level cloud heterogeneity. For pixels with low sub-pixel level cloud heterogeneity (yellowish color) the r_e retrievals from the two methods agree reasonably well. However, for those with significant sub-pixel heterogeneity (marked with black circle in **Fig. 3.2b**), the CER from the bi-spectral method tend to overestimate the results from the polarimetric method. A more in-depth investigation revealed that the polarimetric-based CER retrievals suffer less from the PPHB caused by sub-pixel cloud heterogeneity (see also *Shang et al. 2015*). As aforementioned, the PPHB often causes the bi-spectral method to overestimate the CER. Therefore, the differences between the two method for those outliers in **Fig. 3.2b** is probably because the bi-spectral method suffers more from the PPHB than the polarimetric method.

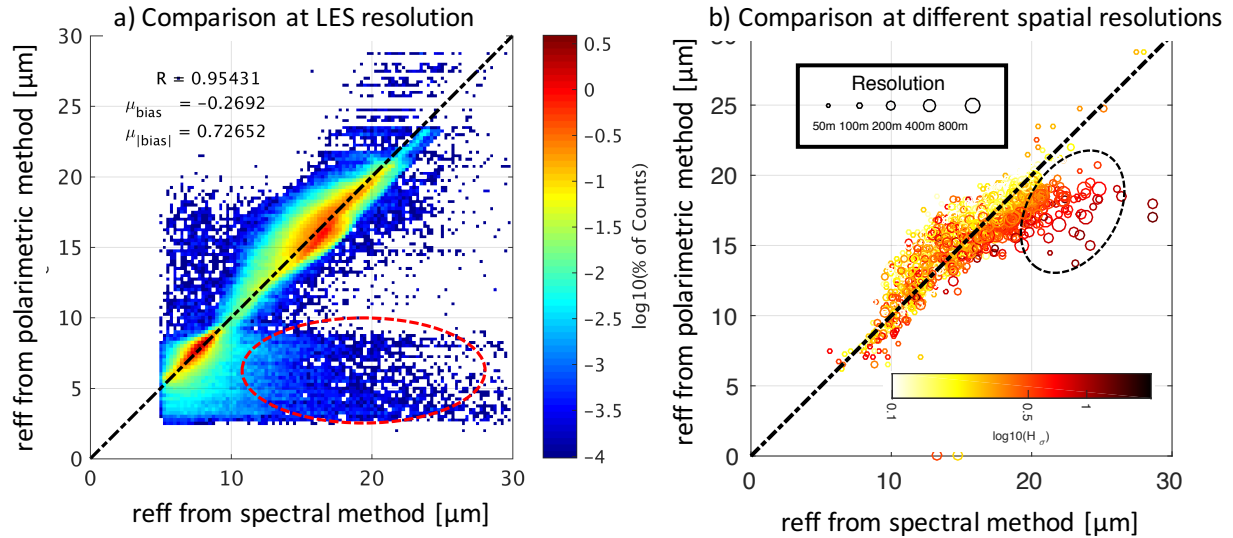


Figure 3.2. a) Joint histogram of CER (re) retrievals based on the bi-spectral and polarimetric retrievals for all LES cases at the native LES resolution. b) Pixel-to-pixel comparison of the CER retrievals based on the bi-spectral and polarimetric methods made at different spatial resolutions. The size of the symbol corresponds to the spatial resolution (i.e., 100 m, 200 m, 400 m and 800 m, increasing respectively) at which the retrievals are made. The symbol color corresponds to the sub-pixel level cloud heterogeneity (yellowish color implies higher homogeneity; reddish color implied higher heterogeneity).

Since the *relative* structure of the polarized reflectance is used to retrieve droplet size information, such retrievals are substantially more robust against 3D-radiative transfer effects, mixed-phase conditions and overlying cirrus or aerosols [Alexandrov *et al.* 2012]. This allows studies on super-cooled liquid drops in mixed-phase cloud conditions [Alexandrov *et al.* 2016] and on drop sizes of broken clouds and clouds possibly affected by overlying aerosols. Such conditions generally lead to unknown biases in retrievals using bi-spectral methods.

Unlike bi-spectral methods, polarimetric retrievals also allow the inference of the width (variance) of the size distribution. In turn, this constrains the ratio of mean particle volume radius to effective radius which is an important and poorly constrained parameter for the estimate of number concentrations from optical thickness and size retrievals [Boers *et al.* 2006].

Limitations: Although our analysis reveals some appealing advantages of the polarimetric method for cloud microphysics retrievals, it also shows some clear limitations of this method that has also been noted and reported in previous studies. *First*, the polarimetric retrievals requires observations of the supernumerary cloud bow around the scattering angle region between 150° and 160° . The capability of a polarimeter to sample this scattering angle range depend on many factors, including solar and viewing angle geometry, the orbit of the satellite and the geolocation of the cloud object. *Secondly*, polarimetric-based retrievals require an angular resolution fine enough to resolve the supernumerary cloud bow. This can be achieved with a single band (e.g., $0.86 \mu\text{m}$) with high angular resolution or through the combination of multi-spectral bands (e.g., $0.86 \mu\text{m}$, $0.64 \mu\text{m}$ and $0.47 \mu\text{m}$) with a moderate angular resolution. Nevertheless, there is a minimum angular resolution requirement for polarimetric based cloud droplet microphysics retrieval. This limit is illustrated in Fig. 3.3 below. As the CDR increases the supernumerary bow becomes narrower and therefore requires a higher angular resolution to resolve. In the figure, the black circles indicate a possible set of angular samples of the cloud bow region of droplet with $\text{CDR}=15 \mu\text{m}$ and $\text{CEV}=0.03$ by a polarimeter with 3° angular resolution. This set of angular samples misses the peak of the

supernumerary lead to a biased CEV retrieval of 0.2. The right panel of the figure shows the minimum angular resolution requirement for resolve the supernumerary bow of different CER with the fixed CEV=0.02. As shown in the figure, to resolve the supernumerary of CER=10 μm , a 4° angular resolution would be enough. However, resolving the supernumerary of a CER \geq 15 μm would require 3° angular resolution. Otherwise, the CEV retrieval is likely to be biased larger than the real value.

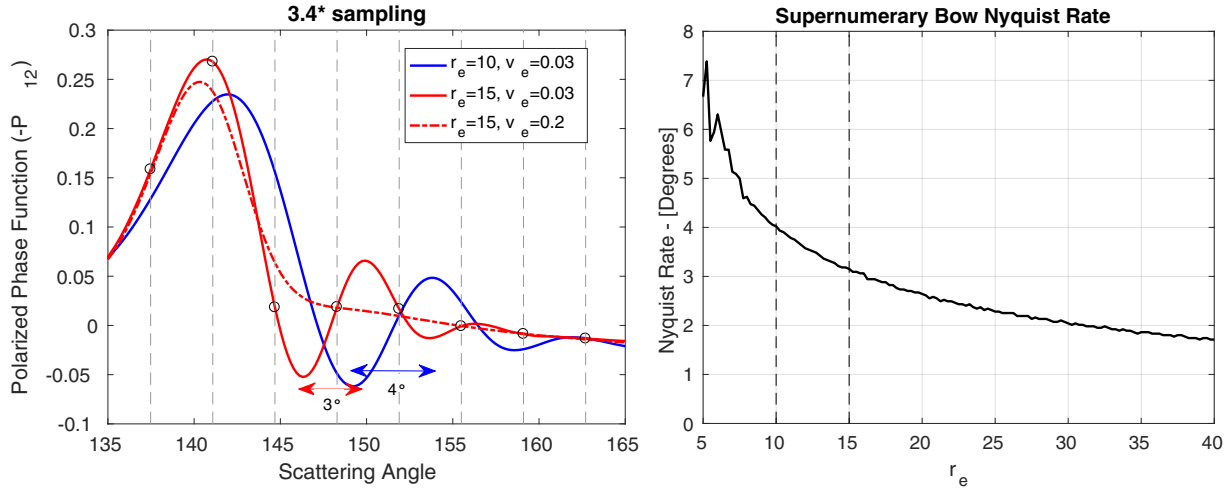


Figure 3.3. (left panel) An example to demonstrate the importance of angular resolution for polarimetric based CEV retrieval. (right panel) the minimum angular resolution requirement for resolve the supernumerary bow of different CER with the fixed CEV=0.02.

Thirdly, as shown in **Fig. 3.1b** the magnitude of the supernumerary peak decreases as the CEV become larger (i.e., broader droplet size distribution). On one hand, this change lends the polarimetric method the ability to retrieve both CER and CEV. On the other hand, it also leads to decreasing sensitivity as CER and CEV increase (somewhat similar to the saturation problem in the bi-spectral method). A recent study by *Shang et al.* [2015] also suggests that the CEV retrieval might be biased toward smaller values when clouds in the FOV of the polarimeter have significant microphysical variability in CER and/or CEV. *Fourth*, because as aforementioned the polarized cloud reflectances consist primarily of single-scattered radiation, the retrieved CER and CEV only represent the cloud microphysics at the uppermost part of the clouds [*Platnick, 2000*]. *Finally*, as with the bi-spectral method, the polarimetric-based method can only be implemented during the daytime.

Summary: We developed a numerical PACE cloud retrieval simulator based on the combination of LES cloud fields and radiative transfer models. This simulator is used to study the advantages and limitations of a notional PACE polarimeter for retrieving the microphysical properties of liquid-phase clouds. Our study confirms two known advantages of polarimeter-based CER retrievals in comparison with the bi-spectral method. First, a significant fraction of optically thin pixels from the LES cases fall into the so-called multiple solution space, where the bi-spectral method is unable to find a single COT and CER solution combination to correspond to the observed cloud reflectances. In contrast, the polarimetric method does not suffer from such a problem if the cloud overlies an ocean surface and polarimetric observations over the cloud bow geometry do not include sun glint contamination. Second, the polarimetric method suffers less from the PPHB caused by sub-pixel cloud heterogeneity that often leads to an overestimation of CER in the bi-spectral method. Our analyses also reveal several limitations of the polarimetric method, chief among which is the capability of the polarimeter to sample the supernumerary cloud bow. This issue should be carefully considered during the instrument design and trade-off studies. Finally, we would like to emphasize

that this analysis is based on synthetic cloud fields from the LES model. Further research is needed to test and confirm these findings, preferably using airborne polarimetric observations.

3.2. Ice Cloud Polarimetric Retrievals

In contrast to liquid clouds, ice crystals in ice clouds are non-spherical and can have a virtually infinite variety of shapes. While the crystalline ice at atmospheric conditions has a fundamental hexagonal lattice structure, in natural clouds ice crystals often appear complex, aggregated and deformed [Bailey and Hallett 2009]. Furthermore, the relative length and width of ice crystal components (i.e. aspect ratios) vary considerably [Um et al. 2015]. Information on the natural variation of ice crystal shape is important because the general shape of an ice crystals determines its scattering properties. Furthermore, microscale surface roughness on the crystals facets also substantially affects ice scattering properties and better constraints on its natural variation is needed. Uncertainties about ice scattering properties and their variation with, e.g., temperature, location, cloud type, add to the uncertainty of the radiative properties of ice clouds implemented in climate models. Moreover, biases in ice scattering properties lead to biases in retrieved ice crystal effective radius and ice cloud optical thickness obtained using bi-spectral methods as mentioned at the end of Sec. 2.3. As shown in **Fig. 3.4**, retrieved ice cloud optical thickness and effective radius scales with the relative bias in $(1 - g)$, where g is the asymmetry parameter of the scattering phase function [Ding et al., 2017; van Diedenhoven et al. 2014].

Multi-directional polarimetric measurements contain information about ice shape and surface roughness and thus about their scattering properties. For a detailed overview of the remote sensing of ice crystals shape and scattering properties we refer to van Diedenhoven [2017]. Ice crystals shape characteristics can be inferred from the polarized reflectances by matching the measured angular variation of polarized reflectances with values simulated using a radiative transfer model assuming various ice crystal optical models. Such optical models are based on the fundamental hexagonal structure of crystal ice.

To date, such methods have been applied to data of POLDER [Doutriaux-Boucher et al. 2000; Knap et al. 2005; van Diedenhoven et al. 2014; Baum et al. 2014] and the airborne Research Scanning Polarimeter [van Diedenhoven et al. 2013]. Many of the past studies aimed to find an ice crystal model that best represents globally averaged data for the use in operational ice cloud optical thickness and effective radius retrievals. Of particular interest for PACE are applications that infer ice scattering properties of a pixel level in order to limit biases in operational ice cloud optical thickness and effective radius retrievals from the OCI instrument. Such pixel-level implementations are presented by, e.g., van Diedenhoven et al. [2012, 2013, 2014], Cole et al. [2014] and Hioki et al. [2016]. Cole et al. [2014] showed that the statistics of ice models and roughness levels vary systematically with latitude. Van Diedenhoven et al. [2012] showed that using simple hexagonal ice prisms with systematically varying aspect ratios and roughness levels as proxies for the complex variety of ice shapes in clouds allows an effective approach to infer ice crystal asymmetry parameters. Applying this approach to POLDER observations of deep convection, van Diedenhoven et al. [2014] showed that aspect ratios, roughness levels and asymmetry parameters vary with cloud top temperature and convective strength. This observed variation implies that ice effective radius and optical thicknesses retrieved using a single ice particle model as currently done for MODIS C6 leads to biases with cloud top temperature, latitude, cloud type and atmospheric conditions.

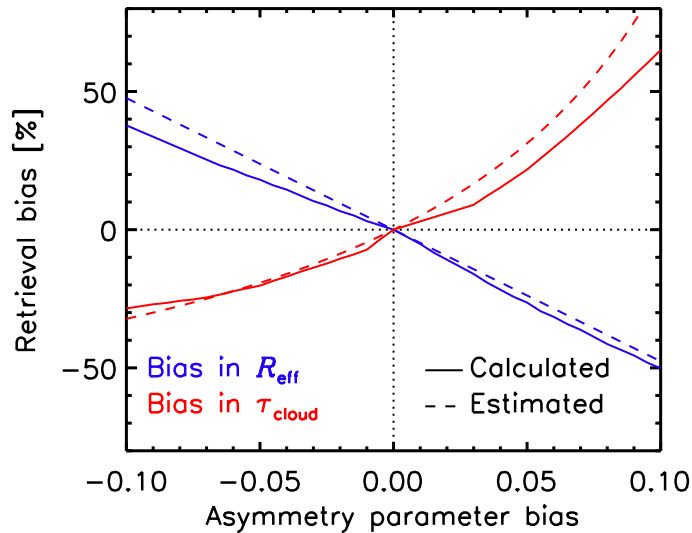


Figure 3.4. Calculated (solid) and estimated (dashed) relative biases in retrieved ice cloud optical thickness (red) and ice effective radius (blue) as a function of absolute bias in assumed asymmetry parameter g at $0.86 \mu\text{m}$. Estimated biases in retrieved ice effective radius and ice cloud optical thickness are equal to the relative bias in $(1 - g)$ and its inverse, respectively. The reference calculations assume a cloud optical thickness of 10, effective radius of $29 \mu\text{m}$ and an asymmetry parameter of 0.79. A solar zenith angle of 24° and a nadir viewing geometry is assumed. Figure reproduced from van Diedenhoven *et al.* [2014].

Advantages: A polarimeter on PACE would allow determination of crystal shape characteristics and asymmetry parameter at ice cloud top at the pixel level. Such retrievals are relatively insensitive to instrument calibration and angular sampling [van Diedenhoven *et al.* 2012] and are expected to be readily applicable to any multi-angle polarimeter. This information can be in turn be used for selection of an appropriate optical model for ice cloud optical thickness and ice effective radius retrievals. Alternatively, when a single optical model is used for the OCI ice cloud optical thickness and ice effective radius retrievals (as done for MODIS C6), the resulting biases can be corrected by scaling the results with the relative bias in $(1 - g)$, as demonstrated in **Fig. 3.4**. In addition, improved statistics about the natural variation of ice crystals shape and roughness can help improving our understanding of ice formation processes, which is currently rather poor. Especially when a “cirrus” band is included on the polarimeter, e.g., located on a water vapor absorption band as discussed in Sec. 2.2, crucial information about particle shape and scattering properties in relatively thin cirrus could be deduced, which is currently challenging with POLDER measurements.

Limitations: Similar for liquid cloud retrievals discussed above, scattering angles in the range $120\text{--}150$ need to be sampled for retrievals of ice crystal shape [van Diedenhoven *et al.* 2012], limiting the retrievals to certain parts of an instrument swath depending on latitude and time of year. Also, since information is obtained from mainly singly scattered light, the resulting scattering properties may be biased towards conditions at the very tops of clouds, while effective radius retrievals are weighted deeper into the cloud.

Summary: Based on previous work, we conclude that addition of a polarimeter on PACE would substantially reduce biases in ice cloud optical thickness and ice effective radius obtained from OCI caused by the assumption of a single invariant ice optical model. In addition, collocated valuable information about ice particle shape will constrain ice formation processes implemented in models. Such retrieval approaches

can be readily applied to any polarimeter with specifications determined for aerosol and/or liquid cloud retrievals.

3.3. Cloud Thermodynamic Phase from Polarimetry

Summary: Spherical liquid drops present at cloud top produce strong angular variations in polarimetry measurements in contrast to ice crystals that have mostly featureless polarized phase functions [Goloub *et al.* 2000; van Diedenhoven *et al.* 2012b]. This allows for a very sensitive detection of liquid drops in cloud tops and hence thermodynamic phase retrievals. As shown by Riedi *et al.* [2010], this approach is especially effective in combination with other information about cloud phase, allowing for a non-binary estimate of thermodynamic phase.

4. References

- Alexandrov, M.D., B. Cairns, C. Emde, A.S. Ackerman, and B. van Dierenhoven, 2012: Accuracy assessments of cloud droplet size retrievals from polarized reflectance measurements by the research scanning polarimeter. *Remote Sens. Environ.*, 125, 92-111, doi:10.1016/j.rse.2012.07.012.
- Alexandrov, M.D., B. Cairns, B. van Dierenhoven, A.S. Ackerman, A.P. Wasilewski, M.J. McGill, J.E. Yorks, D.L. Hlavka, S.E. Platnick, and G.T. Arnold, 2016: Polarized view of supercooled liquid water clouds. *Remote Sens. Environ.*, 181, 96-110, doi:10.1016/j.rse.2016.04.002.
- Ackerman, Steven A., Strabala, Kathleen I., Menzel, W. Paul, Frey, Richard A., Moeller, Christopher C. and Gumley, Liam E. Discriminating clear sky from clouds with MODIS. *J. Geophys. Res.*, Volume 103, 1998, 32,141-32,157.
- Ackerman, A. S., M. P. Kirkpatrick, D. E. Stevens, and O. B. Toon, 2004: The impact of humidity above stratiform clouds on indirect aero- sol climate forcing. *Nature*, 432, 1014–1017.
- Bailey, M. P. and Hallett, J.: A Comprehensive Habit Diagram for Atmospheric Ice Crystals: Confirmation from the Laboratory, AIRS II, and Other Field Studies, *J. Atmos. Sci.*, 66, 2888–2899, doi:10.1175/2009JAS2883.1, 2009.
- Baum, B. A., Yang, P., Heymsfield, A. J., Bansemer, A., Cole, B. H., Merrelli, A., Schmitt, C., and Wang, C.: Ice cloud single-scattering property models with the full phase matrix at wavelengths from 0.2 to 100 μ m, *J. Quant. Spectrosc. Radiat. Transfer*, 146, 123–139, doi:10.1016/j.jqsrt.2014.02.029, 2014.
- Boers, R., J. R. Acarreta, and J. L. Gras, Satellite monitoring of the first indirect aerosol effect: Retrieval of the droplet concentration of water clouds, *J. Geophys. Res.*, 111, D22,208, doi:10.1029/2005JD006838, 2006.
- Bony, S., and J.-L. Dufresne (2005), Marine boundary layer clouds at the heart of tropical cloud feedback uncertainties in climate models, *Geophys. Res. Lett.*, 32, L20806, doi:10.1029/2005GL023851.
- Breon and Goloub, 1998: Cloud droplet effective radius from spaceborne polarization measurements, *Geophys. Res. Lett.*, 25,11, DOI: 10.1029/98GL01221
- Breon and Doutriaux-Boucher, 2005: A comparison of cloud droplet radii measured from space. *IEEE Transactions on Geoscience and Remote Sensing*, Institute of Electrical and Electronics Engineers, 43 (8), pp.1796-1805. <10.1109/TGRS.2005.852838>. <hal-00822138>
- Cahalan, R. and Joseph, 1989.: Fractal Statistics of Cloud Fields. *Mon. Wea. Rev.*, **117**, 261–272, doi: 10.1175/1520-0493(1989)117<0261:FSOCF>2.0.CO;2.
- Cho et al., 2015: Frequency and causes of failed MODIS cloud property retrievals for liquid phase clouds over global oceans, *J. Geophys. Res. Atmos.*, 120, 4132–4154. doi:10.1002/2015JD023161.
- Coddington, O., P. Pilewskie, and T. Vukicevic (2012), The Shannon information content of hyperspectral shortwave cloud albedo measurements: Quantification and practical applications, *J Geophys Res-Atmos*, 117, doi: Artn D04205 10.1029/2011jd016771.
- Coddington, O., K. S. Schmidt, P. Pilewskie, W. J. Gore, R. W. Bergstrom, M. Roman, J. Redemann, P. B. Russell, J. C. Liu, and C. C. Schaaf (2008), Aircraft measurements of spectral surface albedo and its consistency with ground-based and space-borne observations, *J Geophys Res-Atmos*, 113(D17), doi: Artn D17209 10.1029/2008jd010089.

Cole, B. H., Yang, P., Baum, B. A., Riedi, J., and C.-Labonnote, L.: Ice particle habit and surface roughness derived from PARASOL polarization measurements, *Atm. Chem. Phys.*, 14, 3739–3750, doi:10.5194/acp-14-3739-2014, 2014.

Cornet et al., 2010 C. Cornet, L. C-Labonnote, F. Szczap, Three-dimensional polarized Monte Carlo atmospheric radiative transfer model (3DMCPOL): 3D effects on polarized visible reflectances of a cirrus cloud, *Journal of Quantitative Spectroscopy and Radiative Transfer*, 111, <http://doi.org/10.1016/j.jqsrt.2009.06.013>.

Davis and Marshak 2010: Solar radiation transport in the cloudy atmosphere: a 3D perspective on observations and climate impacts. *Reports on Progresses in Physics*, v73, no2, [Note(s): 026801.1-026801.70]

Ding et al., Validation of quasi-invariant ice cloud radiative quantities with MODIS satellite-based cloud property retrievals, *JQSRT*, 194(2017) 47–57, 2017.

Doutriaux-Boucher, M., Buriez, J., Brogniez, G., C.-Labonnote, L., and Baran, A. J.: Sensitivity of retrieved POLDER directional cloud optical thickness to various ice particle models, *Geophys. Res. Lett.*, 27, 109, doi:10.1029/15999GL010870, 2000.

Eplee, R. E., J. Sun, G. Meister, F. S. Patt, T. C. Stone, X. Xiong, and C. R. McClain (2011), Cross Calibration of SeaWiFS and MODIS Using On-Orbit Observations of the Moon, *Applied Optics*, Vol. 50, No. 2, 120–133.

Fischer, J., and H. Grassl (1991), Detection of Cloud-Top Height from Backscattered Radiances within the Oxygen a-Band .1. Theoretical-Study, *J Appl Meteorol*, 30(9), 1245-1259, doi: Doi 10.1175/1520-0450(1991)030<1245:Docthf>2.0.Co;2.

Franz, B.A., E.J. Kwiatkowska, G. Meister, and C. McClain (2008). Moderate Resolution Imaging Spectroradiometer on Terra: limitations for ocean color applications, *J. Appl. Rem. Sens.*, 2, 023525.

Goloub, P., M. Herman, H. Chepfer, J. Riedi, G. Brogniez, P. Couvert, and G. Seze (2000), Cloud thermodynamical phase classification from the POLDER spaceborne instrument, *J Geophys Res-Atmos*, 105(D11), 14747–14759, doi: Doi 10.1029/1999jd901183.

Hall, D.K., G. Riggs, V. Salomonson (1995). Development of methods for mapping global snow cover using Moderate Resolution Imaging Spectroradiometer (MODIS) data. *Remote Sensing of Environment*, 54, pp. 127–140.

de Haan, J. F.; Bosma, P. B.; Hovenier, J. W. 1987: The adding method for multiple scattering calculations of polarized light. *Astronomy and Astrophysics* (ISSN 0004-6361), v183, no. 2, Sept. 1987, p. 371–391

Heidinger, Andrew K., Evan, Amato T., Foster, Michael J. and Walther, Andi. A naive Bayesian cloud-detection scheme derived from CALIPSO and applied within PATMOS-x. *J. Appl. Meteor. Climatol.*, Volume 51, Issue 6, 2012, 1129–1144.

Heidinger, A. K., C. O'Dell, R. Bennartz, and T. Greenwald (2006), The successive-order-of-interaction radiative transfer model. Part I: Model development, *J Appl Meteorol Clim*, 45(10), 1388–1402, doi: 10.1175/Jam2387.1.

Hioki, S., Yang, P., Baum, B. A., Platnick, S., Meyer, K. G., King, M. D., and Riedi, J.: Degree of ice particle surface roughness inferred from polarimetric observations, *Atm. Chem. Phys.*, 16, 7545–7558, doi:10.5194/acp-16-7545-2016, 2016.

Holz, R. E., et al., Resolving ice cloud optical thickness biases between CALIOP and MODIS using infrared retrievals, *Atmos. Chem. Phys.*, v15, no. 20, pp. 29455–29495, 2015, doi: 10.5194/acpd-15-29455-2015.

- King, M. D. (1987), Determination of the Scaled Optical-Thickness of Clouds from Reflected Solar-Radiation Measurements, *J Atmos Sci*, 44(13), 1734–1751, doi: 10.1175/1520-0469(1987)044<1734:Dotsot>2.0.Co;2.
- Knap, W. H., C.-Labonnote, L., Brogniez, G., and Stammes, P.: Modeling total and polarized reflectances of ice clouds: evaluation by means of POLDER and ATSR-2 measurements, *Appl. Opt.*, 44, 4060, doi:10.1364/AO.44.004060, 2005.
- Levy, R., L. Remer, R. Kleidman, S. Mattoo, C. Ichoku, R. Kahn, and T. F. Eck, 2010. Global evaluation of the Collection 5 MODIS dark-target aerosol products over land. *Atmos. Chem. Phys.* **10**, 10399–10420.
- Lyapustin, A. et al. (2014), Scientific impact of MODIS C5 calibration degradation and C6+ improvements, *Atmos. Meas. Tech.*, 7(12), 4353–4365, doi:10.5194/amt-7-4353-2014.
- Marshak, A., S. Platnick, T. Várnai, G. Wen, and R. F. Cahalan 2006, Impact of three-dimensional radiative effects on satellite retrievals of cloud droplet sizes, *J. Geophys. Res.*, 111, D09207, doi:10.1029/2005JD006686.
- Menzel, W. P., Frey, Richard A, Zhang, H., Wylie, Donald P., Moeller, Chris C, Holz, Robert E., Maddux, Brent, Baum, Bryan A., Strabala, Kathy, I., and Gumley, Liam E. MODIS global cloud top pressure and amount estimation: Algorithm description and results. *J. Appl. Meteor. Climatol.*, **47**, 2008, 1175–1198.
- Menzel, W. P., R. A. Frey, E. E. Borbas, B. A. Baum, G. Cureton, and N. Bearson (2016), Reprocessing of HIRS Satellite Measurements from 1980 to 2015: Development toward a Consistent Decadal Cloud Record, *J Appl Meteorol Clim*, 55(11), 2397–2410, doi: 10.1175/Jamc-D-16-0129.1.
- Meyer, K., and S. Platnick (2010), Utilizing the MODIS 1.38 μm channel for cirrus cloud optical thickness retrievals: Algorithm and retrieval uncertainties, *J. Geophys. Res.*, 115, D24209, doi:10.1029/2010JD014872.
- Nakajima, T., and M. D. King (1990), Determination of the Optical-Thickness and Effective Particle Radius of Clouds from Reflected Solar-Radiation Measurements .1. Theory, *J Atmos Sci*, 47(15), 1878-1893, doi: Doi 10.1175/1520-0469(1990)047<1878:Dotota>2.0.Co;2.
- PACE Science Definition Team (2018), Pre-Aerosol, Clouds, and ocean Ecosystem (PACE) Mission Science Definition Team Report. Rep., NASA Goddard Space Flight Center, Greenbelt, MD.
- Platnick, S., et al. MODIS Collection 6 Cloud Optical Property User Guide, http://modis-atmos.gsfc.nasa.gov/_docs/C6MOD06OPUserGuide.pdf, 141 pages, Oct. 2015.
- Platnick, S., K. Meyer, M. D. King, G. Wind, N. Amarasinghe, B. Marchant, G. T. Arnold, Z. Zhang, P. A. Hubanks, R. E. Holz, P. Yang, W. L. Ridgway, and J. Riedi, 2017: The MODIS cloud optical and microphysical products: Collection 6 updates and examples from Terra and Aqua. *IEEE Trans. Geosci. Remote Sens.*, **55**, 502–525, doi:10.1109/TGRS.2016.2610522.
- Platnick, S., S. A. Ackerman, R., Frey, R. Holz, A. Heidinger, Y. Li, S. Wanzong, K. Meyer, G. Wind, N. Amarasinghe, B. Marchant, B., and T. Arnold (2015), MODAWG: MODIS-VIIRS Product Continuity for Cloud Mask, Cloud-Top & Optical Properties, 2015 MODIS Science Team Meeting, https://modis.gsfc.nasa.gov/sci_team/meetings/201505/presentations/plenary/platnick.pdf
- Platnick, S., 2000: Vertical photon transport in cloud remote sensing problems. *J. Geophys. Res.*, 105, D18, 22,919.
- Riedi, J., B. Marchant, S. Platnick, B. A. Baum, F. Thieuleux, C. Oudard, F. Parol, J.-M. Nicolas, and P. Dubuisson, 2010: Cloud thermodynamic phase inferred from merged POLDER and MODIS data. *Atmos. Chem. Phys.*, 10, 11851–11865, doi:10.5194/acp-10-11851-2010.

- Rossow, W. B. and L. C. Garder, 1993: Cloud detection using satellite measurements of infrared and visible radiances for ISCCP. *Journal of Climate*, Volume 6 (12), 2341–2369.
- Sayer, A. M., et al. (2016), In-Situ and Remotely-Sensed Observations of Biomass Burning Aerosols at Doi Ang Khang, Thailand during 7-SEAS/BASELInE 2015, *Aerosol Air Qual Res*, 16(11), 2786–2801, doi: 10.4209/aaqr.2015.08.0500.
- Schaaf, C. B., J. C. Liu, F. Gao, and A. H. Strahler (2011), Aqua and Terra MODIS Albedo and Reflectance Anisotropy Products, *Remote Sens Digit Im*, 11, 549-561, doi: 10.1007/978-1-4419-6749-7_24.
- Shang, H., Chen, L., Bréon, F. M., Letu, H., Li, S., Wang, Z., and Su, L.: Impact of cloud horizontal inhomogeneity and directional sampling on the retrieval of cloud droplet size by the POLDER instrument, *Atmos. Meas. Tech.*, 8, 4931–4945, doi:10.5194/amt-8-4931-2015, 2015.
- Sun, J., X. Xiong, and J. Butler (2012a), NPP VIIRS on-orbit calibration and characterization using the moon, *Proc. of SPIE*, Vol. 8510, 85101I, 2012, doi: 10.1117/12.939933.
- Sun, J., A. Angal, X. Xiong, H. Chen, X. Geng, A. Wu, T. Choi, and M. Chu (2012b), MODIS reflective solar bands calibration improvements in Collection 6, *Proc. of SPIE*, Vol. 8528, 85280N, doi: 10.1117/12.979733.
- Um, J., McFarquhar, G. M., Hong, Y. P., Lee, S.-S., Jung, C. H., Lawson, R. P., and Mo, Q.: Dimensions and aspect ratios of natural ice crystals, *Atm. Chem. Phys.*, 15, 3933–3956, doi:10.5194/acp-15-3933-2015, 2015
- Van Diedenhoven, B., B. Cairns, I.V. Geogdzhayev, A.M. Fridlind, A.S. Ackerman, P. Yang, and B.A. Baum, 2012: Remote sensing of ice crystal asymmetry parameter using multi-directional polarization measurements. Part I: Methodology and evaluation with simulated measurements. *Atmos. Meas. Tech.*, 5, 2361-2374, doi:10.5194/amt-5-2361-2012.
- Van Diedenhoven, B., A. M. Fridlind, A. S. Ackerman, and B. Cairns (2012b), Evaluation of hydrometeor phase and ice properties in cloud-resolving model simulations of tropical deep convection using radiance and polarization measurements, *J. Atmos. Sci.*, 69(11), 3290–3314, doi:10.1175/JAS-D-11-0314.1
- Van Diedenhoven, B., B. Cairns, A.M. Fridlind, A.S. Ackerman, and T.J. Garrett, 2013: Remote sensing of ice crystal asymmetry parameter using multi-directional polarization measurements — Part 2: Application to the Research Scanning Polarimeter. *Atmos. Chem. Phys.*, 13, 3185–3203, doi:10.5194/acp-13-3185-2013.
- Van Diedenhoven, B., A.M. Fridlind, B. Cairns, and A.S. Ackerman, 2014: Variation of ice crystal size, shape and asymmetry parameter in tops of tropical deep convective clouds. *J. Geophys. Res. Atmos.*, 119, no. 20, 11809–11825, doi:10.1002/2014JD022385.
- Van Diedenhoven, B., 2017: Remote sensing of crystal shapes in ice clouds. In *Cloud Remote Sensing*. A. Kokhanovsky, Ed., Light Scattering Reviews 12. Springer Praxis, in press.
- Várnai, T. and A. Marshak, 2002: Observations of Three-Dimensional Radiative Effects that Influence MODIS Cloud Optical Thickness Retrievals. *J. Atmos. Sci.*, 59, 1607–1618, doi: 10.1175/1520-0469(2002)059<1607:OOTDRE>2.0.CO;2.
- Vukicevic, T., O. Coddington, and P. Pilewskie (2010), Characterizing the retrieval of cloud properties from optical remote sensing, *J Geophys Res-Atmos*, 115, doi: Artn D20211 10.1029/2009jd012830.
- Wang, C., S. Ding, P. Yang, B. Baum, and A. E. Dessler (2012), A new approach to retrieving cirrus cloud height with a combination of MODIS 1.24- and 1.38- μm channels, *Geophys. Res. Lett.*, 39, L24806, doi:10.1029/2012GL053854.

- Wang, W., and C. Cao (2016), Monitoring the NOAA Operational VIIRS RSB and DNB Calibration Stability Using Monthly and Semi-Monthly Deep Convective Clouds Time Series, *Remote Sensing*, 8(1), 32–19, doi:10.3390/rs8010032.
- Wang, P., P. Stammes, R. van der A, G. Pinardi, and M. van Roozendaal (2008), FRESCO+: an improved O-2 A-band cloud retrieval algorithm for tropospheric trace gas retrievals, *Atmos Chem Phys*, 8(21), 6565-6576.
- Werner, F., G. Wind, Z. B. Zhang, S. Platnick, L. Di Girolamo, G. Y. Zhao, N. Amarasinghe, and K. Meyer (2016), Marine boundary layer cloud property retrievals from high-resolution ASTER observations: case studies and comparison with Terra MODIS, *Atmos Meas Tech*, 9(12), 5869-5894, doi: 10.5194/amt-9-5869-2016.
- Wood, R., K. K. Comstock, C. S. Bretherton, C. Cornish, J. Tomlinson, D. R. Collins, and C. Fairall, 2008: Open cellular structure in marine stratocumulus sheets. *J. Geophys. Res.*, 113, D12207. doi:10.1029/2007JD009371
- Xiong, X., A. Angal, A. Wu, D. Link, X. Geng, W. Barnes, and V. Salomonson (2016), Sixteen Years of Terra MODIS On-orbit Operation, Calibration, and Performance, Sensors, Systems, and Next-Generation Satellites Xx, 10000, doi: Unsp 10000v 10.1117/12.2241352.
- Yang, P. et al., Spectrally consistent scattering, absorption, and polarization properties of atmospheric ice crystals at wavelengths from 0.2 to 100 μm , *J. Atmos. Sci.*, v70, no. 1, pp. 330–347, Jan. 2013.
- Zhang, Z., and S. Platnick (2011), An assessment of differences between cloud effective particle radius retrievals for marine water clouds from three MODIS spectral bands, *J. Geophys. Res.*, 116, D20215, doi:10.1029/2011JD016216.
- Zhang, Z., F. Werner, H.-M. Cho, G. Wind, S. Platnick, A. S. Ackerman, L. Di Girolamo, and A. Marshak (2016), A framework for quantifying the impacts of sub-pixel reflectance variance and covariance on cloud optical thickness and effective radius retrievals based on bi-spectral method. *J. Geophys. Res. Atmos.*, 121, no. 12, 7007–7025, doi:10.1002/2016JD024837.
- Zhang, Z. B., A. S. Ackerman, G. Feingold, S. Platnick, R. Pincus, and H. W. Xue (2012), Effects of cloud horizontal inhomogeneity and drizzle on remote sensing of cloud droplet effective radius: Case studies based on large-eddy simulations, *J Geophys Res-Atmos*, 117, doi: Artn D1920810.1029/2012jd017655.

Previous Volumes in This Series

- Volume 1**
April 2018 ACE Ocean Working Group recommendations and instrument requirements for an advanced ocean ecology mission
- Volume 2**
May 2018 Pre-Aerosol, Clouds, and ocean Ecosystem (PACE) Mission Science Definition Team Report
- Volume 3**
October 2018 Polarimetry in the PACE mission: Science Team consensus document

